Mode competition of rotating waves in reflection-symmetric Taylor–Couette flow

By J. ABSHAGEN[1], J. M. LOPEZ[2], F. MARQUES[3]
AND G. PFISTER[1]

[1]Institute of Experimental and Applied Physics, University of Kiel, 24105 Kiel, Germany

[2]Department of Mathematics and Statistics, Arizona State University, Tempe, AZ 85287, USA

[3]Departament de Física Aplicada, Universitat Politècnica de Catalunya,
08034, Barcelona, Spain

We report on the results of a combined experimental and numerical study on mode interactions of rotating waves in Taylor–Couette flow. Our work shows that rotating waves which originate at a Hopf bifurcation from the steady axisymmetric Taylor vortex flow interact with this axisymmetric flow in a codimension-two fold-Hopf bifurcation. This interaction gives rise to an (unstable) low-frequency modulated wave via a subcritical Neimark–Sacker bifurcation from the rotating wave. At higher Reynolds numbers, a complicated mode interation between stable modulated waves originating at a different Neimark–Sacker bifurcation and a pair of symmetrically related rotating waves that originate at a cyclic pitchfork bifurcation is found to organize complex Z_2-symmetry breaking of rotating waves via global bifurcations. In addition to symmetry breaking of rotating waves via a (local) cyclic pitchfork bifurcation, we found symmetry breaking of modulated waves via a saddle-node-infinite-period (SNIP) global bifurcation. Tracing these local and global bifurcation curves in Reynolds number/aspect ratio parameter space toward their apparant merging point, unexpected complexity arises in the bifurcation structure involving non-symmetric two-tori undergoing saddle-loop homoclinic bifurcations. The close agreement between the numerics and the experiment is indicative of the robustness of the observed complex dynamics.

1. Introduction

Bifurcation theory has long been a very useful tool in the analysis of complex nonlinear hydrodynamics. Examples arise from convection, such as Rayleigh–Bénard convection (Tuckerman & Barkley 1988; Kevrekidis *et al.* 1994) and electroconvection in liquid crystals (Peacock & Mullin 2001), and from rotating fluids, such as Taylor–Couette flow (Mullin 1991, 1993; Egbers & Pfister 2000; Lopez, Marques & Fernando 2004*a*) and lid-driven cavities (Blackburn & Lopez 2002; Marques, Lopez & Shen 2002; Lopez *et al.* 2002*a*; Nore *et al.* 2003; Lopez & Marques 2004). Symmetries determine the solution set close to a bifurcation and symmetry-breaking bifurcations have been found to be an important mechanism for the appearance of multiple solutions in fluid flows (Benjamin & Mullin 1982; Crawford & Knobloch 1991; Chossat & Iooss 1994). In symmetric systems, any solution to which a symmetry operator is applied is also a solution, and if that solution is unchanged then the solution is symmetric. Otherwise, the solutions are distinct and symmetrically

related. In such systems, bifurcations can be interpreted as either symmetry breaking (restoring) or symmetry preserving.

Complex hydrodynamics is often organized by global bifurcations which originate from the local bifurcation structure. In particular, homoclinic and heteroclinic bifurcations have been found to play a crucial role in hydrodynamics. Mode interaction provides a generic mechanism to organize homoclinic and heteroclinic bifurcations in the vicinity of a multiple local bifurcation point. Moreover, low-frequency dynamics often arise from a Neimark–Sacker bifurcation (Hopf-like bifurcation from a limit cycle) as a result of mode interaction. Therefore, in-depth knowledge of mode interaction is important for the understanding of the organization of complex dynamics in fluid flows.

Taylor–Couette flow between two concentric rotating cylinders is one of the classical hydrodynamic systems for the study of bifurcation events and the transition to turbulence. The 'standard' set-up consists of a rotating inner cylinder and stationary outer cylinder and endwalls. The symmetry group of this system is $SO(2) \times Z_2$, corresponding to invariance to rotations about the axis, $SO(2)$, and reflection about the axial mid-plane, Z_2. There are three non-dimensional governing parameters: the Reynolds number Re, the radius ratio η, and the length-to-gap aspect ratio Γ.

From the pioneering work of Benjamin and Mullin (Benjamin 1978a, b; Mullin 1982) it has become evident that endwalls are dominant for the bifurcation behaviour of the Taylor–Couette system. In fact, the axial translation invariance that is inherent in models assuming periodic boundary conditions is completely destroyed by the presence of endwalls; the transition to axisymmetric Taylor cells is smooth with increasing Reynolds number, rather than the pitchfork of revolution bifurcation found in the idealized periodic model (Crawford & Knobloch 1991). With physical endwall boundary conditions, the primary bifurcations to axisymmetric Taylor vortex flows are saddle-node bifurcations that are organized by codimension-two cusp bifurcations resulting from mode interchange processes between flow states with $2N$ and $2N + 2$ cells, with $2N$ being of order Γ.

Subsequent numerical and experimental work revealed that crucial mechanisms for the organization of the axisymmetric flow are Z_2 symmetry-breaking pitchfork bifurcations (Mullin, Toya & Tavener 2002). Mode interaction of symmetry-breaking bifurcations and saddle-node (fold) bifurcations originating from mode interchange processes give rise to low-frequency dynamics resulting from a Hopf bifurcation (Mullin, Tavener & Cliffe 1989) and the appearance of complex dynamics due to Shil'nikov mechanisms (Price & Mullin 1991; Mullin 1991). The loss of axisymmetry, i.e. $SO(2)$ symmetry breaking, occurs primarily via Hopf bifurcations which lead to rotating waves with azimuthal wavenumbers m (Knobloch 1994), and they may be either reflection symmetric or have a spatio-temporal reflection symmetry composed of a reflection together with an appropriate rotation (DiPrima & Swinney 1981; Tagg 1994). Rotating waves are periodic solutions which are special in the sense that the time-dependence is a drift in the direction of the $SO(2)$ symmetry, i.e. a precession, and are better described as relative equilibria. Near a relative equilibrium the drift dynamics associated with the precession is trivial and decouples from the dynamics orthogonal to the relative equilibrium. As a result the bifurcations from relative equilibria can be analysed in two steps, describing first the bifurcations associated with the orthogonal dynamics, and then adding the corresponding drift along the rotating wave (Krupa 1990). Subsequent instabilities of rotating waves to quasi-periodic flows have been explored experimentally and found to lead to a multitude of very-low-frequency states via a variety of global bifurcations, the details depending on
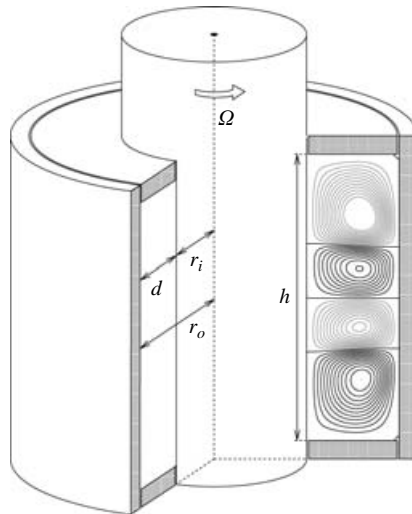
FIGURE 1. Schematic of the flow apparatus.

all three governing parameters (Gerdts *et al.* 1994; von Stamm *et al.* 1996; Abshagen, Pfister & Mullin 2001; Abshagen *et al.* 2005).

In this study, we investigate both numerically and experimentally the mode competition of rotating waves. The aim is to clarify the origin of low-frequency dynamics and the role global bifurcations play in Taylor–Couette flow. In order to reduce the number of possible multiple solutions and their interactions, the aspect ratio Γ has to be choosen to be small, between about 3 and 4, so that the mode competition is between basic states with two and four cells. A fixed wide-gap radius ratio of $\eta = 0.5$ is used throughout this study. In the wide-gap regime the sequences of bifurcations are more spaced out in (Γ, Re) parameter space than they are in the narrow-gap $\eta \to 1$ regime.

2. Navier–Stokes equations and the numerical scheme

We consider an incompressible flow confined in an annulus of inner radius r_i and outer radius r_o and length h, driven by the constant rotation of the inner cylinder at Ω rad s^{-1}. The system is non-dimensionalized using the gap, $d = r_o - r_i$, as the length scale and the diffusive time across the gap, d^2/ν, as the time scale (where ν is the fluid's kinematic viscosity). The equations governing the flow are the Navier–Stokes equations together with initial and boundary conditions. In cylindrical coordinates, (r, θ, z), we denote the non-dimensional velocity vector and pressure by $\boldsymbol{u} = (u, v, w)^T$ and p, respectively. The system is governed by three non-dimensional parameters, two geometric and one dynamic:

$$\text{radius ratio:} \qquad \eta = r_i/r_o,$$
$$\text{annulus aspect ratio:} \quad \Gamma = h/d,$$
$$\text{Reynolds number:} \quad Re = \Omega d r_i/\nu.$$

In this study, we fix $\eta = 0.5$ and vary Re and Γ, both in the numerical computations and the experiments. A schematic of the flow geometry, with an insert showing the streamlines for a steady axisymmetric solution at $Re = 400$, $\Gamma = 3.10$ is given in figure 1.

The governing equations are the (non-dimensional) Navier–Stokes equations

$$\partial \boldsymbol{u}/\partial t + (\boldsymbol{u} \cdot \nabla)\boldsymbol{u} = -\nabla p + \nabla^2 \boldsymbol{u}, \qquad \nabla \cdot \boldsymbol{u} = 0, \tag{2.1}$$

subject to no-slip boundary conditions. Specifically, $u = v = w = 0$ on all stationary boundaries, i.e. at the outer cylinder, $r = r_o/d = 1/(1-\eta) = 2$, and the top and bottom endwalls $z = \pm 0.5h/d = \pm 0.5\Gamma$. On the rotating inner cylinder, $r = r_i/d = \eta/(1-\eta) = 1$, $u = w = 0$ and $v = Re$.

To solve (2.1), a stiffly stable semi-implicit second-order projection scheme is used, where the linear terms are treated implicitly while the nonlinear terms are explicit (see Lopez & Shen 1998; Lopez, Marques & Shen 2002b, for more details, including the treatment of discontinuous boundary conditions). For the space variables, we use a Legendre–Fourier approximation. More precisely, the azimuthal direction is discretized using a Fourier expansion with $N_\theta + 1$ modes corresponding to azimuthal wavenumbers $m = 0, 1, 2, \ldots N_\theta$, while the axial and radial directions are discretized with a Legendre expansion. For example, the spectral expansion for the axial velocity component is

$$w(r, \theta, z, t) = \sum_{i=0}^{N_z} \sum_{j=0}^{N_r} \sum_{k=-N_\theta}^{N_\theta} w_{i,j,k}(t) \phi_i \left(\frac{2z}{\Gamma} \right) \psi_j \left(2r - \frac{1+\eta}{1-\eta} \right) \mathrm{e}^{\mathrm{i}k\theta}, \tag{2.2}$$

where ϕ_i and ψ_j are appropriate combinations of Legendre polynomials in order to satisfy boundary conditions.

The spectral convergence of the code in the radial and axial directions has already been extensively described in Lopez & Shen (1998) for $m = 0$; the convergence properties in these directions are not affected by $m \neq 0$. For the convergence in azimuth, we note that the mode of instability being investigated here leads to rotating waves with azimuthal wavenumber $m = 1$. This numerical scheme has been used to investigate similar dynamics in Taylor–Couette flows with different boundary conditions and parameter regimes where resolution issues have been addressed (Lopez & Marques 2003; Lopez, Marques & Shen 2004b). The results presented here have 48 and 64–96 Legendre modes in the radial and axial directions, respectively, and up to 11 Fourier modes in θ (resolving up to azimuthal wavenumber $m = 10$); the time step used is $\delta t \in [10^{-5}, 10^{-4}]$.

3. Experimental technique

The experimental set-up of the Taylor–Couette system used for this study consists of a fluid (silicon oil with kinematic viscosity $\nu = 10.2\,\mathrm{mm}^2\,\mathrm{s}^{-1}$, with an absolute uncertainty of $\pm 0.1\,\mathrm{mm}^2\,\mathrm{s}^{-1}$) confined in the gap between two concentric cylinders. The outer cylinder and the top and bottom endwalls were held fixed. A phase-locked loop (PLL) circuit controlled the angular velocity of the inner cylinder, Ω, to an accuracy of better than one part in 10^{-4} in the short term and 10^{-7} in the long-term average. The inner cylinder was machined from stainless steel with radius $r_i = (12.50 \pm 0.01)\,\mathrm{mm}$, while the outer cylinder, with $r_o = (25.00 \pm 0.01)\,\mathrm{mm}$, was made from optically polished glass. The temperature of the fluid was thermostatically controlled to $(21.00 \pm 0.01)\,^\circ\mathrm{C}$. The apparatus was located in an air-controlled cabinet and the laboratory was air conditioned. The distance between the endwalls, h, is adjustable within an accuracy of $0.01\,\mathrm{mm}$. Laser Doppler velocimetry (LDV) was used for measurements of the local flow velocity and laser light-sheet techniques were used for flow visualization. Further technical details of the experimental apparatus
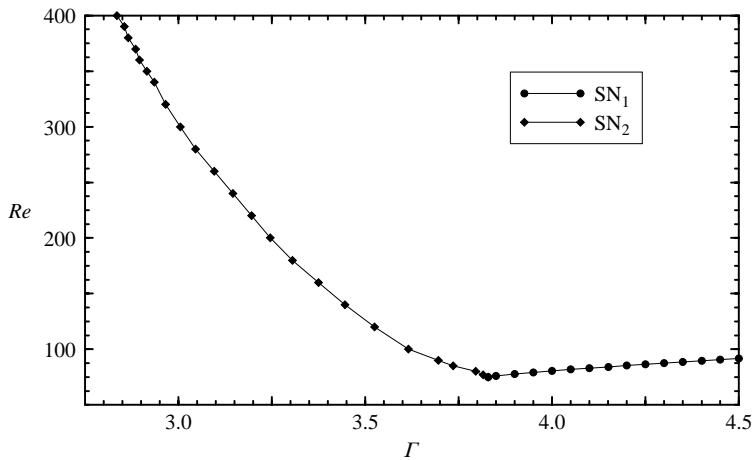
FIGURE 2. Saddle-node bifurcation curves SN_1 and SN_2, where s_1 and s_2 each undergo saddle-node bifurcations, respectively.

and measurement procedures can be found in Gerdts *et al.* (1994) and von Stamm *et al.* (1996).

4. Basic flow states and their saddle-node bifurcations

For $\eta = 0.5$ and Γ of order 4, there is a broad wedged-shaped region in (Γ, Re) parameter space, delimited by a pair of saddle-node bifurcation curves which meet at a codimension-two cusp point at $(\Gamma = 3.81, Re = 76)$. In this region there are three basic-state solutions (i.e. solutions which are steady and $SO(2) \times Z_2$ symmetric, $SO(2)$ being invariance to rotations about the axis and Z_2 invariance to reflection through the mid-plane $z = 0$); two are stable (s_1 and s_2, described below) and the third (s_M) is unstable. Figure 2 shows the loci of these saddle-node bifurcation curves. The two stable steady states are distinguished by the number of jets of angular momentum that issue from the boundary layer on the rotating inner cylinder; one has a single jet, denoted s_1, and the other has two, denoted s_2. Contour plots of the three computed components of velocity and the corresponding streamlines, as well as a flow visualization photograph of s_1 and s_2, are shown in figures 3 and 4, respectively, both at $Re = 330$, $\Gamma = 3.0$, $\eta = 0.5$. For $\Gamma > 3.81$, s_2 is smoothly connected to the unique basic state as $Re \to 0$ (the Stokes flow limit), which is characterized by Ekman vortices on the endwalls, and s_1 comes into existence with increasing Re as the saddle-node curve SN_1 is crossed. For $\Gamma < 3.81$, s_1 is connected smoothly with the Stokes flow limit and s_2 comes into existence with increasing Re as the saddle-node curve SN_2 is crossed.

In this study, we shall focus on the dynamics involved in the competition between bifurcated states from s_2 for $\Gamma < 3.8$. In this parameter regime, a rich dynamics manifests itself as s_2 is followed towards the saddle-node bifurcation SN_2.

5. Hopf bifurcation to a rotating wave

The basic state s_2 loses stability via a symmetry-breaking Hopf bifurcation as Re is increased beyond about 400 for $\Gamma \in (2.9, 3.4)$. There are four possible types of symmetry which the resulting limit cycle may have, distinguished by the actions of the
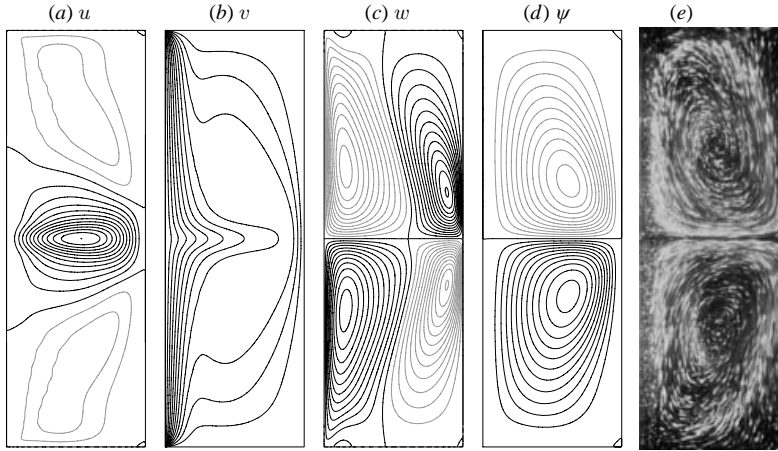
FIGURE 3. Axisymmetric steady state, s_1, at $Re = 330$, $\Gamma = 3.0$, $\eta = 0.5$; computed with $N_z = 64$, $N_r = 48$, $\delta t = 10^{-4}$; there are twelve positive (black) and negative (grey) contours with the following levels: (a) $u \in [-125, 125]$, (b) $v \in [0, 400]$, (c) $w \in [-80, 80]$, and (d) $\psi \in [-15, 15]$; (e) corresponding visualization of the experimental flow.
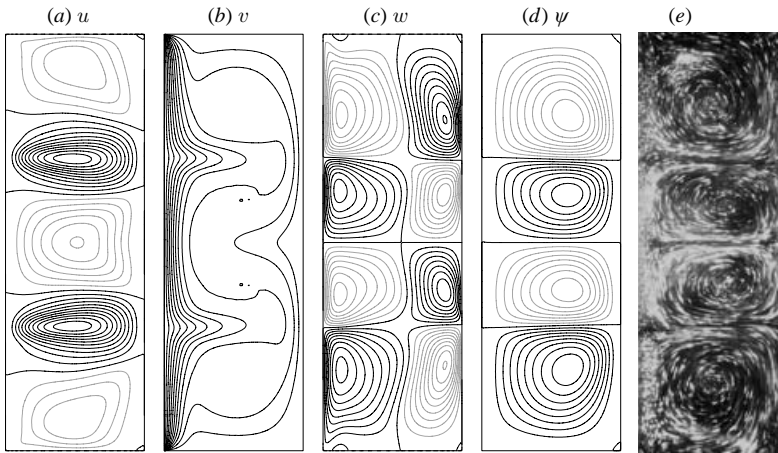

FIGURE 4. As figure 3 but for axisymmetric steady state, s_2.

two symmetry subgroups Z_2 and $SO(2)$, and characterized by $s = \pm 1$, associated with the action of Z_2, and $m \in \mathbb{Z}$ related to the action of $SO(2)$ (Lopez & Marques 2003, 2004). If $m = 0$, the action of $SO(2)$ is trivial, and the limit cycle is axisymmetric; if $s = +1$, the action of Z_2 is trivial, and the limit cycle is point-wise reflection symmetric. If $m \neq 0$, the action of $SO(2)$ is equivalent to a temporal evolution, and the limit cycle is a rotating wave with azimuthal wavenumber m. If $s = -1$, the action of Z_2 is equivalent to a half-period temporal evolution.

The Hopf bifurcation at which s_2 loses stability, H_2, leads to a limit cycle with $m = 1$ and $s = -1$, a type IV limit cycle (Lopez & Marques 2003, 2004). It is a rotating wave with precession period $\tau = 2\pi/\omega$ where ω is the Hopf frequency, and we denote it RW$_S$. RW$_S$ is invariant to a rotation about the axis through π composed with a reflection about the mid-plane. This is an involution; applying this twice is equivalent to the action of the identity, i.e. it is a Z_2 symmetry. Figure 5 shows contours in
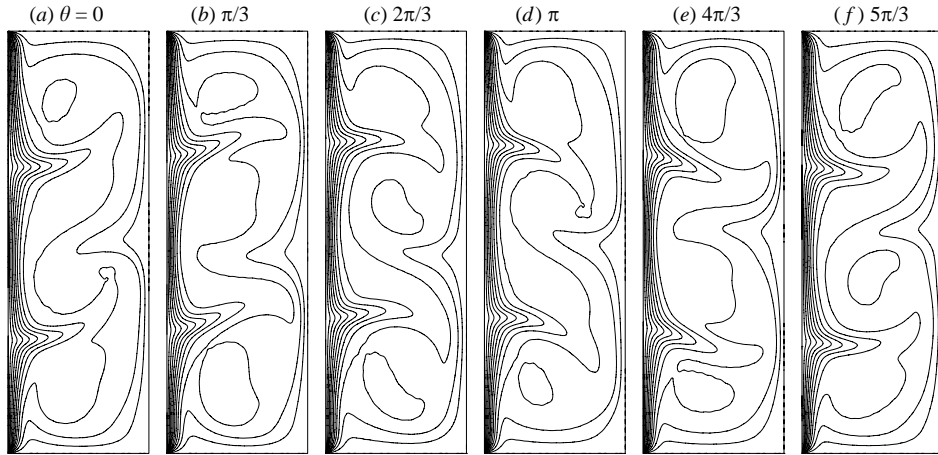
FIGURE 5. Contours of v in various meridional planes, as indicated, for RW$_S$ at $Re = 700$, $\Gamma = 3.0$, $\eta = 0.5$; computed with $N_z = 96$, $N_r = 48$, $N_\theta = 10$, $\delta t = 2 \times 10^{-5}$. There are twelve equispaced contours with the levels $v \in [0, Re]$.
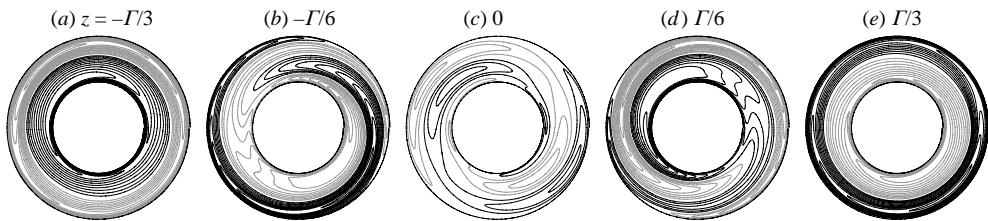

FIGURE 6. Contours of w, at various axial levels as indicated, for RW$_S$ at $Re = 700$, $\Gamma = 3.0$, $\eta = 0.5$; computed with $N_z = 96$, $N_r = 48$, $N_\theta = 10$, $\delta t = 2 \times 10^{-5}$. There are twelve positive (black) and negative (gray) contours with the levels $w \in [-150, 150]$.

various meridional planes around the annulus of the azimuthal velocity of a RW$_S$ solution at $Re = 700$ and $\Gamma = 3.0$. The in-phase tilts of the two jets issuing from the boundary on the rotating inner cylinder are clearly evident, as is the Z_2 symmetry composed of a rotation through π together with a reflection about $z = 0$. Note also that the rotation through π (half a spatial period rotation) is equivalent a temporal evolution through half the precession period of the rotating wave.

The non-axisymmetric nature of RW$_S$ is associated with the tilting of the jets, which in the basic state s_2 issue from the boundary layer at constant z (compare with figure 4b). Figure 6 shows contours of the axial velocity of the RW$_S$ solution shown in figure 5 at various axial levels z. Note that the jets issue from the boundary layer at about $z = \pm \Gamma/6$, and at these z levels the solution is most non-axisymmetric (the $m = 1$ nature of the tilt is quite evident), and away from the jets (e.g. for $z = \pm \Gamma/3$), RW$_S$ is very nearly axisymmetric. This type of $m = 1$ rotating wave state is often referred to as a tilt wave.

Figure 7 shows contours of the azimuthal velocity of the RW$_S$ solution shown in figures 5 and 6, on (a) the meridional plane $\theta = 0$, and (b) a cylindrical surface (θ, z) at $r = r_i/d + 0.3$, projected on a plane and compressed in azimuth by a factor of four in order to better display the structure of the tilt wave. The figure shows that both jets are in phase, that RW$_S$ is a mode $m = 1$ solution, and also clearly displays the
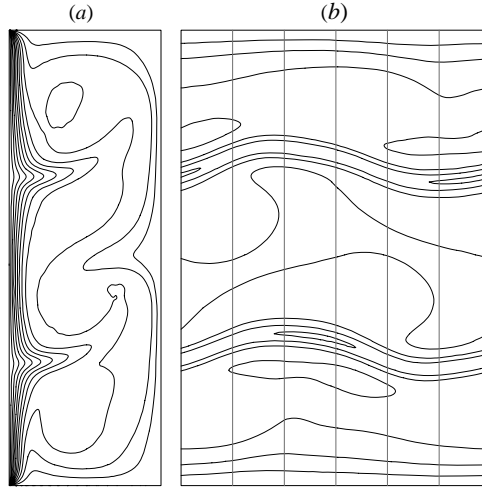
FIGURE 7. Contours of v on (a) the meridional plane $\theta = 0$, and (b) the cylindrical projection (θ, z) at $r = r_i/d + 0.3$, for RW$_S$ at $Re = 700$, $\Gamma = 3.0$, $\eta = 0.5$. Vertical lines at angles $\theta = j\pi/3$ for $j = 1$ to 5 are included in (b), which correspond to the meridional planes used in figure 5. There are twelve equispaced contours with the levels $v \in [0, Re]$.

Z_2 symmetry of the RW$_S$: invariance under a z-reflection followed by a rotation of π around the axis: $\theta \to \theta + \pi$.

For systems with larger Γ, for which the basic state has more than two outgoing jets, their primary Hopf bifurcations (i.e. the first Hopf bifurcation from the basic state as parameters are varied) lead to rotating waves ($m \neq 0$) with the jets tilted out-of-phase, i.e. $s = +1$ for an even number of jets and $s = -1$ for an odd number of jets. The two-jet case s$_2$ studied here is the only one for which the primary Hopf bifurcation leads to a rotating wave with the jets tilted in-phase, $s = -1$; the secondary Hopf bifurcation (i.e. the second Hopf bifurcation from the now unstable basic state) with $s = +1$, from the basic state s$_2$, has not been found experimentally (or numerically). Experiments over a wide range of Γ (up to $\Gamma = 32$) have shown that for basic states with three or more jets, the out-of-phase mode is always the primary rotating wave, and that the critical Re for the Hopf bifurcation is independent of the number of jets but depends on Γ (von Stamm *et al.* 1996). For the single-jet basic state s$_1$ at $\Gamma = 0.5$, Hopf bifurcations with both $s = +1$ and $s = -1$ were found to compete as primary bifurcations when the radius ratio is larger than that considered here, $\eta \sim 0.67$ compared with the present $\eta = 0.5$ (Lopez & Marques 2003).

Figure 8 shows the saddle-node bifurcation curve SN$_2$, together with the Hopf bifurcation curve H$_2$ at which RW$_S$ bifurcates from s$_2$, and a Neimark–Sacker bifurcation curve NS$_2$ at which RW$_S$ becomes unstable. The solid (dotted) lines with the filled (open) symbols are the numerically (experimentally) determined curves.

The precession periods τ close to the onset of the Hopf bifurcation are shown in figure 9; the filled squares are the experimentally determined periods, and the open diamonds are the computationally determined values. The precession period is a small fraction of the viscous diffusion time across the annular gap, varying between about 3.5% and 2.5% of the viscous time for Γ between about 2.9 and 3.5. We have found that the precession period varies much less with Re than it does with Γ. The agreement between the numerics and the experiments for both the critical values of the parameters and for the critical eigenvalue (inversely proportional to the
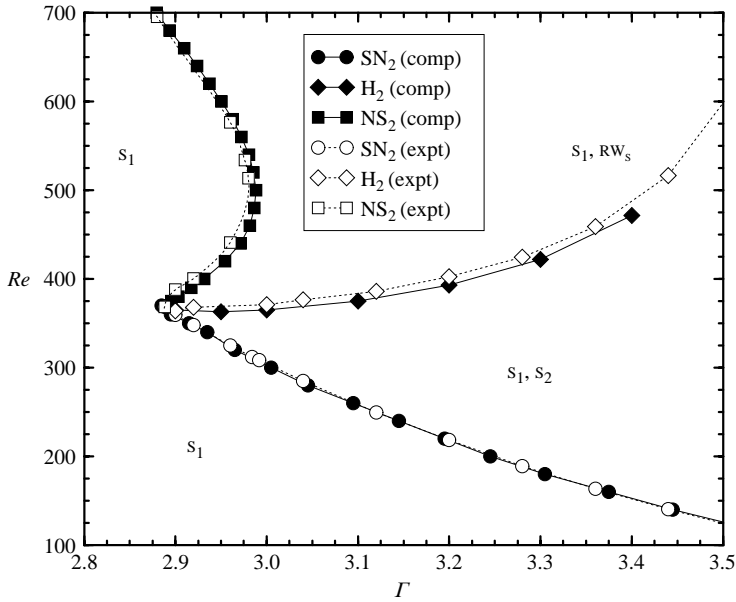
FIGURE 8. Bifurcation curves in (Γ, Re) space, including the saddle-node SN_2 (only shown up to the fold-Hopf point), the Hopf H_2, and the Neimark–Sacker NS_2 bifurcation curves. The stable solutions in each region are indicated. The solid (dotted) lines with the filled (open) symbols are the numerically (experimentally) determined curves.
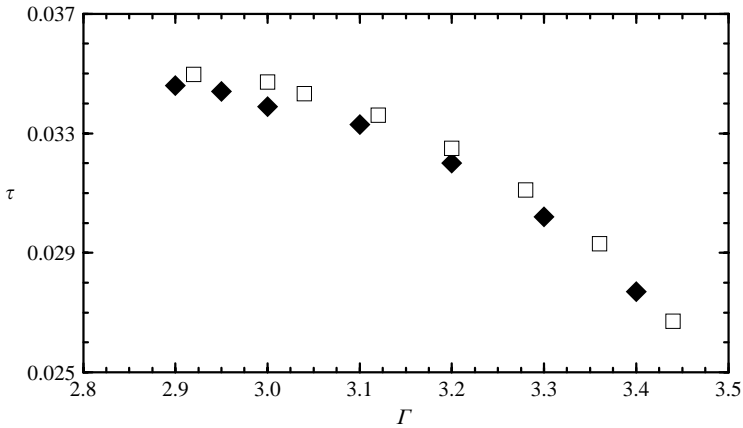

FIGURE 9. Variation with Γ of the precession period of the rotating wave $\mathrm{RW_S}$, τ, very close to the Hopf bifurcation, in viscous time units d^2/ν, as determined computationally (solid diamonds) and experimentally (open squares).

precession period at onset) is indicative of the precision of the experiments and the accuracy of the numerics.

The Hopf bifurcation H_2 is supercritical; at onset, the amplitude squared of the rotating wave grows linearly with distance in parameter space from the bifurcation curve, and the precession period is only a weak function of the parameters. To estimate the amplitude squared, we introduce global measures of the solution which
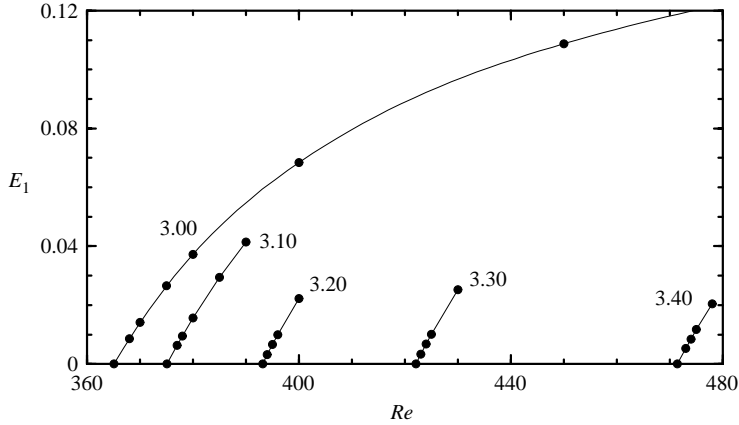
FIGURE 10. Variation of E_1 of RW$_\text{S}$ with Re for Γ as indicated.

are the (scaled) kinetic energies in the mth Fourier modes of the solution:

$$E_m = \frac{1}{Re^2} \int_{z=-\Gamma/2}^{z=\Gamma/2} \int_{r=1}^{r=2} \boldsymbol{u}_m \cdot \overline{\boldsymbol{u}}_m r \, dr \, dz, \qquad (5.1)$$

where $\boldsymbol{u}_m$ is the mth Fourier mode of the velocity field. For rotating waves, E_m is constant in time. For RW$_\text{S}$, $m = 1$; in figure 10 we plot E_1 as a function of Re for various $\Gamma \in [3.00, 3.40]$, which cover the Hopf bifurcation curve H$_2$ shown in figure 8. The linear growth of E_1 from zero with increasing Re is clearly evident. While we do not have experimental data measuring the 'amplitude' of RW$_\text{S}$ for the present range of Γ, the supercriticality of the Hopf bifurcation leading to RW$_\text{S}$ in other parameter regimes has been determined experimentally in Gerdts *et al.* (1994).

The SN$_2$ saddle-node bifurcation curve and the H$_2$ Hopf bifurcation curve coincide at a codimension-two fold-Hopf bifurcation point at ($\Gamma = 2.89$, $Re = 360$), from which a Neimark–Sacker (NS$_2$) bifurcation curve also emerges (see figure 8). The nonlinear dynamics in the neighbourhood of this fold-Hopf point are now considered.

6. Fold-Hopf bifurcation

In the neighbourhood of a codimension-two fold-Hopf bifurcation, the infinite-dimensional phase space of the Taylor–Couette problem admits a three-dimensional centre manifold parameterized by a coordinate x, an amplitude ρ and an angle ϕ. The normal form is given by (Kuznetsov 1998)

$$\left. \begin{array}{l} \dot{x} = -\mu_1 + x^2 + \sigma\rho^2, \\ \dot{\rho} = \rho(-\mu_2 + \chi x + x^2), \\ \dot{\phi} = \omega, \end{array} \right\} \qquad (6.1)$$

where μ_1 and μ_2 are the normalized bifurcation parameters related to Re and Γ. The signs in (6.1) have been chosen in order to easily compare with our representation of the dynamics in (Γ, Re)-parameter space. The eigenvalues at the fold-Hopf bifurcation point $\mu_1 = \mu_2 = 0$ are zero and $\pm i\omega$. The coefficients in the normal form are $\sigma = \pm 1$, and χ and ω that depend on the parameters μ_1 and μ_2 and satisfy certain non-degeneracy conditions in the neighbourhood of the bifurcation: $\omega \neq 0$, $\chi \neq 0$. The ϕ equation describes a rotation around the x-axis with constant angular velocity,
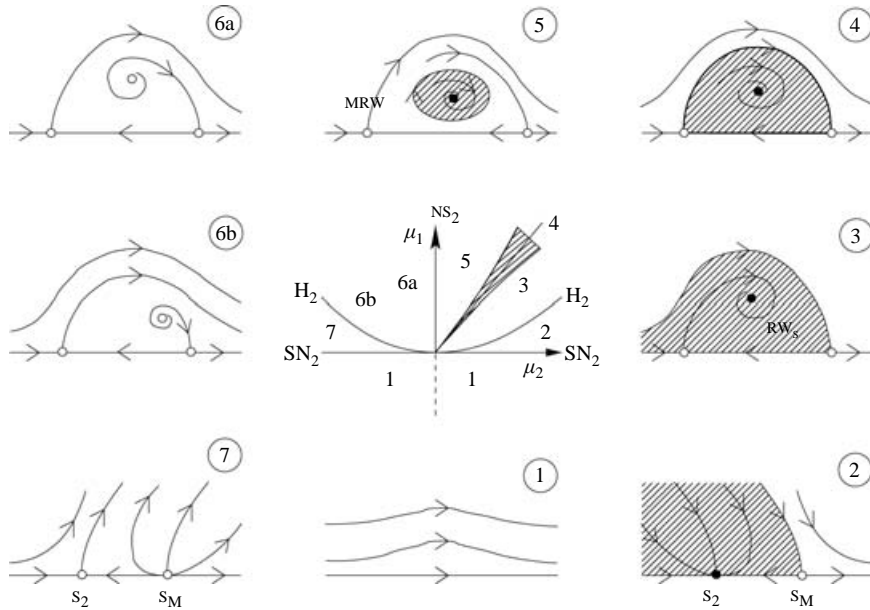
FIGURE 11. Bifurcation diagram of the fold-Hopf bifurcation, in normal form variables, corresponding to the present flow. Filled (•) and open (◦) dots correspond to stable and unstable solutions respectively, μ_1 and μ_2 are the two bifurcation parameters, SN_2 is a saddle-node bifurcation curve, H_2 is the Hopf bifurcation curve, NS_2 is the Neimark–Sacker bifurcation curve, and 4 is the horn region of complex dynamics; the straight line inside region 4 is the heteroclinic connection predicted by the formal normal form (6.1) and shown in panel 4 as a thick line.

$\phi = \phi_0 + \omega t$. Thus, to understand the bifurcations in (6.1), we only need to consider the planar system for (x, ρ), with $\rho \geqslant 0$, which is independent of ϕ. This system has three fixed points:

(a) $s_2 = (-\sqrt{\mu_1}, 0)$, which exists for $\mu_1 > 0$ and is stable iff $\mu_2 + \chi\sqrt{\mu_1} < 0$;

(b) $s_M = (\sqrt{\mu_1}, 0)$, which exists for $\mu_1 > 0$ and is unstable;

(c) $RW_S = (\mu_2/\chi + O(\mu_2^2), \sqrt{\sigma(\mu_1 - \mu_2^2/\chi^2)} + O(\mu_2^3))$, which exists for $\sigma(\mu_1 - \mu_2^2/\chi^2) > 0$ and is stable iff $\sigma\chi < 0$ and $\mu_2\chi < 0$.

The normal form (6.1) admits distinct dynamic scenarios, depending on the values of χ and σ. A comprehensive description of these scenarios is given in Kuznetsov (1998). Since the periodic solution RW_S in our flow is stable and exists for $\mu_2 > 0$, then $\sigma = +1$. For this scenario, the bifurcation diagram and corresponding phase portraits in the neighbourhood of the fold-Hopf point where SN_2 and H_2 coincide are presented in figure 11. For $\sigma\chi < 0$, complex solutions exist in the neighbourhood of the fold-Hopf bifurcation point, including two-tori, heteroclinic structures, homoclinic solutions and more. The normal form (6.1) is generic in the sense that no symmetry considerations were imposed in its derivation. Although our system has $SO(2) \times Z_2$ symmetry, this does not alter the normal form in our case since the $SO(2)$ group does not affect the normal form (see Iooss & Adelmeyer 1998), and for the region in parameter space under investigation, the Z_2 symmetry is not broken (the steady state s_2 is point-wise Z_2 symmetric and the rotating wave RW_S is set-wise Z_2 symmetric).

The phase portraits in figure 11 are projections onto (x, ρ); rotation about the horizontal axis x recovers angle (ϕ) information. The x-axis is the axisymmetric-invariant subspace. The fixed points on the x-axis (s_2 and s_M) correspond to steady

axisymmetric states. The off-axis fixed point corresponds to a limit cycle (the rotating wave RW_S). The limit cycle in region 5 is an unstable modulated rotating wave MRW. The parametric portrait in the centre of the figure consists of seven distinct regions separated by different bifurcation curves. Initial conditions starting in region 1 ($\mu_1 < 0$) evolve to far away states, not related to the fold-Hopf bifurcation (in our system, they evolve towards the s_1 steady state). As μ_1 changes sign for $\mu_2 > 0$, the saddle-node bifurcation curve SN_2 is crossed and a pair of fixed points appears: s_2 stable and s_M unstable (region 2); the basin of attraction of s_2 is shown shaded in the figure. On further increasing μ_1, the stable fixed point s_2 undergoes a supercritical Hopf bifurcation (H_2), becomes unstable and a limit cycle (the rotating wave RW_S) emerges (region 3); its basin of attraction is shown shaded in the figure. If we continue increasing μ_1, according to the analysis of the normal form (6.1), a heteroclinic invariant two-dimensional manifold appears, as a result of the stable and unstable manifolds of s_2 and s_M coinciding (the thick line in the phase portrait 4). The basin of attraction of RW_S (shaded region) is delimited by the heteroclinic connection. This connection occurs along the straight line in the middle of region 4. However, this invariant sphere is a highly degenerate heteroclinic structure and high-order terms in the normal form destroy it (see discussions in Wiggins 1988; Guckenheimer & Holmes 1983; Kuznetsov 1998). In a generic system, instead of a single bifurcation curve associated with this invariant sphere, there is a horn-shaped region about it (the hatched region 4). Generically, the unstable invariant manifold of s_2 and the stable invariant manifold of s_M intersect transversally. This transversal intersection begins and ends in two heteroclinic tangency curves which are the limiting curves of the horn region 4. Inside region 4, the dynamics can be extremely complex, including an infinity of two-tori, solutions homoclinic and heteroclinic to both unstable fixed points, cascades of saddle-node and period-doubling bifurcations, and chaos. However, in this fold-Hopf scenario, the only local stable solution of the system is RW_S and the complex dynamics associated with the horn are transient. On leaving the horn region (crossing the line 4 in the normal form), an unstable two-torus MRW appears from a heteroclinic bifurcation between s_1 and s_M. The two-torus surrounds RW_S, and the basin of attraction of RW_S is the interior of the two-torus. On decreasing μ_2 in region 5, the two-torus MRW collapses in on RW_S at a subcritical Neimark–Sacker bifurcation NS_2. On further decreasing μ_2 into regions 6 and 7, all local equilibria are unstable and trajectories evolve away from these regions of phase space to s_1.

Both the experiments and the numerical simulations find that on decreasing Γ for fixed Re in the range $Re \in (400, 700)$, RW_S loses stability at a subcritical Neimark–Sacker bifurcation, NS_2 (shown in figure 8 as open and filled squares for the experimentally and numerically determined curve, respectively). Since no stable solution arises from the subcritical NS_2, the resulting modulated rotating wave only occurs as a transient. Figure 12 shows a time series of the low-pass-filtered LDV measurements of the axial velocity at $z = 0$ and $r = r_i + 1.5$ mm (LDV provides a voltage which is proportional to the Doppler-shift of the light scattered by small latex particle suspended in the flow, which is proportional to the velocity in the direction of view), that was recorded experimentally after Re had been slightly increased from a value where RW_S was stable to $Re = 405$, at $\Gamma = 2.94$, i.e. from region 5 to region 6 in figure 11. It shows the transient response of the flow to a (small) increase in Re. Since the precession frequency of the RW_S is filtered out by the low-pass filter with cut-off frequency $f = 0.2$ Hz, the oscillatory response corresponds to the modulation frequency of the unstable modulated rotating wave. The low modulation frequency provides experimental evidence that the Neimark–Sacker bifurcation curve has been
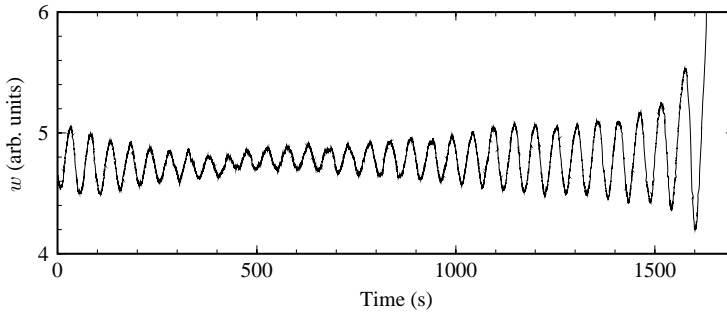
FIGURE 12. Time series of axial velocity w recorded in the axial midplane at a distance of 1.5 mm from the inner cylinder and low-pass filtered with a cut-off frequency $f = 0.2$ Hz. The low-frequency component of a transient modulated wave at $\Gamma = 2.94$ and $Re = 405$ is depicted. The end of the time series indicates the transition to s_1. The viscous time is $d^2/\nu \approx 15.3$ s.

crossed. Since the bifurcation is subcritical, this modulated flow state occurs only as a transient. The end of the time series shown in figure 12 indicates the transition from a transient modulated wave to the far-off state s_1.

In the region between the NS_2 and H_2 curves, RW_S is the only locally stable state (s_1 is also stable, but it is 'far away' in phase space from the equilibria associated with the s_2 solution manifold), until Re is larger than about 640. In the following section, the stability of RW_S for $Re > 640$ is explored.

7. Instabilities of the Z_2-symmetric rotating wave RW_S

The codimension-one bifurcations that a Z_2-symmetric limit cycle can undergo correspond to either a real Floquet multiplier $\mu = +1$ or a pair of complex-conjugate Floquet multipliers $\mu = e^{\pm i\omega}$ crossing the unit circle. The period-doubling bifurcation with $\mu = -1$ is inhibited due to the presence of the Z_2 symmetry (Swift & Wiesenfeld 1984). When Z_2 symmetry is broken, the $\mu = +1$ bifurcation is a pitchfork of limit cycles (cyclic pitchfork, CP), which can be either super- or subcritical, and a pair of (symmetrically related) non-symmetric limit cycles is born. If the Z_2 symmetry is preserved, the $\mu = +1$ bifurcation is a saddle-node bifurcation of cycles (cyclic fold, CF). In the Neimark–Sacker bifurcation, NS_s with $\mu = e^{\pm i\omega}$, a modulated rotating wave is born; this quasi-periodic solution evolves on a two-torus, T_s^2, which is Z_2-symmetric although the individual quasi-periodic solutions on it are not (Kuznetsov 1998).

The Z_2-symmetric limit cycle in the present Taylor–Couette flow, RW_S, undergoes two of the aforementioned bifurcations: for $\Gamma > 3.18$, Z_2 symmetry is broken and a pair of asymmetric limit cycles, RW_A, appear in a cyclic pitchfork bifurcation; for $\Gamma < 3.18$ a Neimark–Sacker bifurcation takes place, resulting in a Z_2-symmetric two-torus T_s^2 with quasi-periodic solutions MRW_S. The loci of these two bifurcation curves are plotted in figure 13 where their numerically and experimentally determined locations in (Γ, Re) space are shown with filled and open circles respectively. Also shown in the figure are bifurcation curves with $\Gamma \sim 3.16$ that divide the parameter space into regions where MRW_S and RW_A exist; these will be described and discussed in §8.
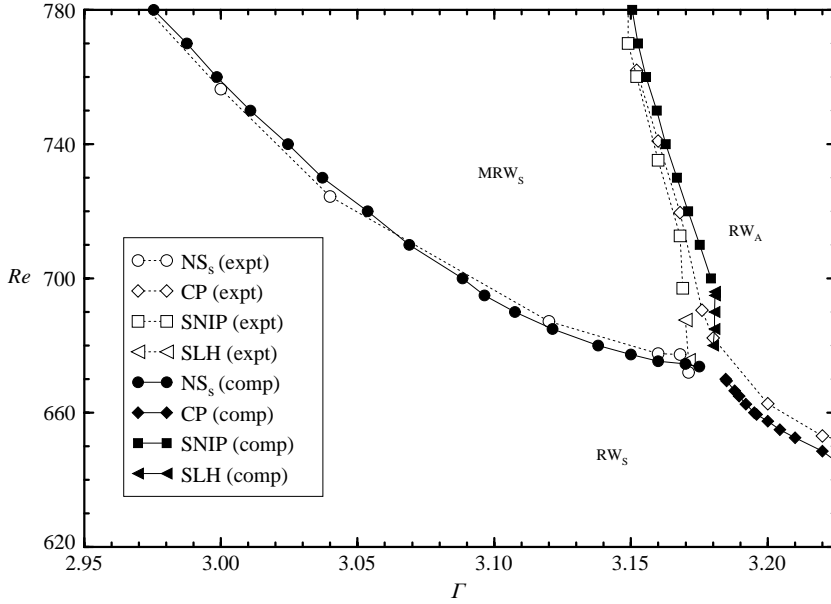
FIGURE 13. Bifurcation curves in (Re, Γ) space: NS_s is the curve of Neimark–Sacker bifurcations at which the RW_S becomes unstable and spawns the Z_2-symmetric T_s^2 with MRW_S solutions; CP is the curve of cyclic pitchfork bifurcations at which RW_S becomes unstable and a pair of Z_2-conjugate RW_A is spawned; SNIP is the saddle-node-infinite-period bifurcation curve on which saddle-nodes of RW_A occur upon T_s^2; SLH is a curve of saddle-loop homoclinic bifurcations at which MRW_S becomes heteroclinic to a pair of saddle Z_2-conjugate rotating waves. Curves with open (filled) symbols are determined experimentally (numerically).

7.1. *Neimark–Sacker bifurcation of* RW_S

The Neimark–Sacker bifurcation NS_s of RW_S occurs for $\Gamma \lesssim 3.17$ and a modulated rotating wave MRW_S is spawned. For rotating waves, the modal kinetic energies E_m are constant in time, and for modulated rotating waves, E_m are time-periodic. The amplitude and period of the oscillations in E_1 for MRW_S are global measures of the modulation amplitude squared (the kinetic energy is a squared quantity) and modulation period of MRW_S, denoted ΔE_1 and τ_2, respectively.

Figure 14 shows the variation with Re of (*a*) ΔE_1 and (*b*) τ_2 of MRW_S for various Γ. Note that for the smaller values of Γ ($\lesssim 3.15$), ΔE_m grows linearly with Re and the modulation period τ_2 varies very slowly with Re, indicative of the supercritical nature of the Neimark–Sacker bifurcation. However, for $\Gamma = 3.16$, the figures show that the nature of the bifurcation changes; the amplitude loses its linearity very soon after the bifurcation, and the period varies significantly at onset. In fact, the figure suggests that the period is becoming unbounded at onset. Figure 15 shows the modulation period near onset of the Neimark–Sacker bifurcation as a function of Γ; τ_2 increases significantly as Γ approaches 3.18, and follows an inverse square-root law, $\tau_2 \sim 1/\sqrt{|\Gamma - \Gamma_c|}$, as shown by the straight line fit.

Since MRW_S bifurcates from a Z_2-symmetric limit cycle RW_S, then the two-torus upon which MRW_S evolves is also (set-wise) Z_2-symmetric (Kuznetsov 1998). The modal energies, E_m, being squared quantities, mask this symmetry; time series of E_m for MRW_S show a periodicity equal to $\tau_2/2$. In order to reveal the symmetry, we plot in figure 16(*a*) a phase portrait of MRW_S projected onto the plane (W^-, W^+) where $W^\pm$
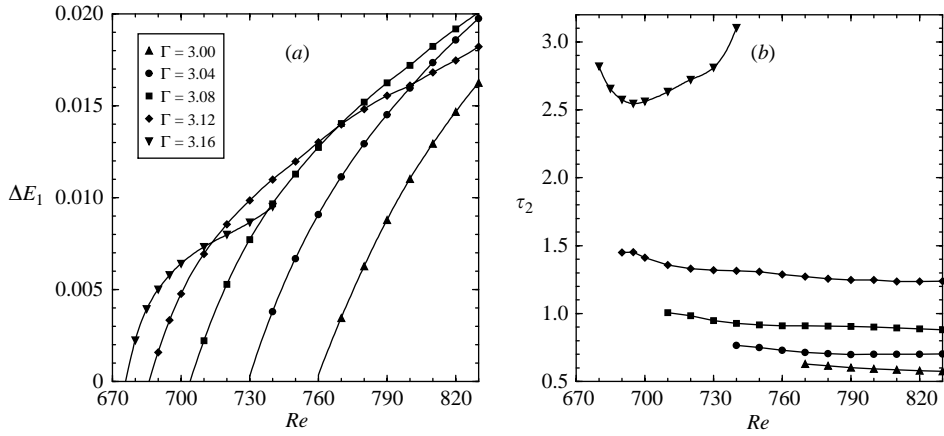
FIGURE 14. Variation with Re of (a) the modulation amplitude ΔE_1 and (b) the modulation period τ_2 of MRW$_S$ for various Γ as indicated.
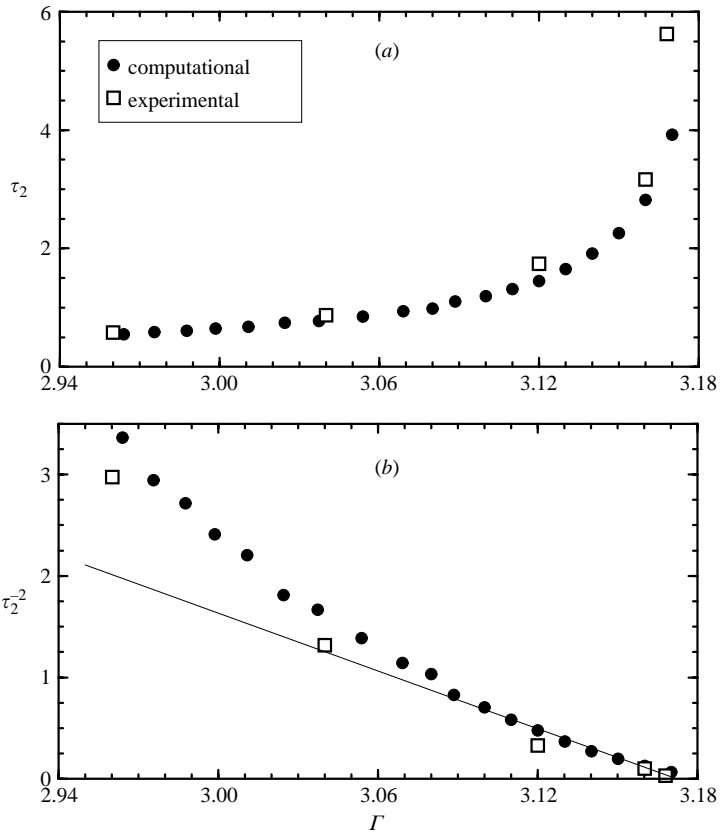

FIGURE 15. Variation with Γ of the modulation period of MRW$_S$, τ_2, very close to the Neimark–Sacker bifurcation, in viscous time units d^2/ν, determined numerically and experimentally. The straight line is a fit to the nine computed points with larger Γ.
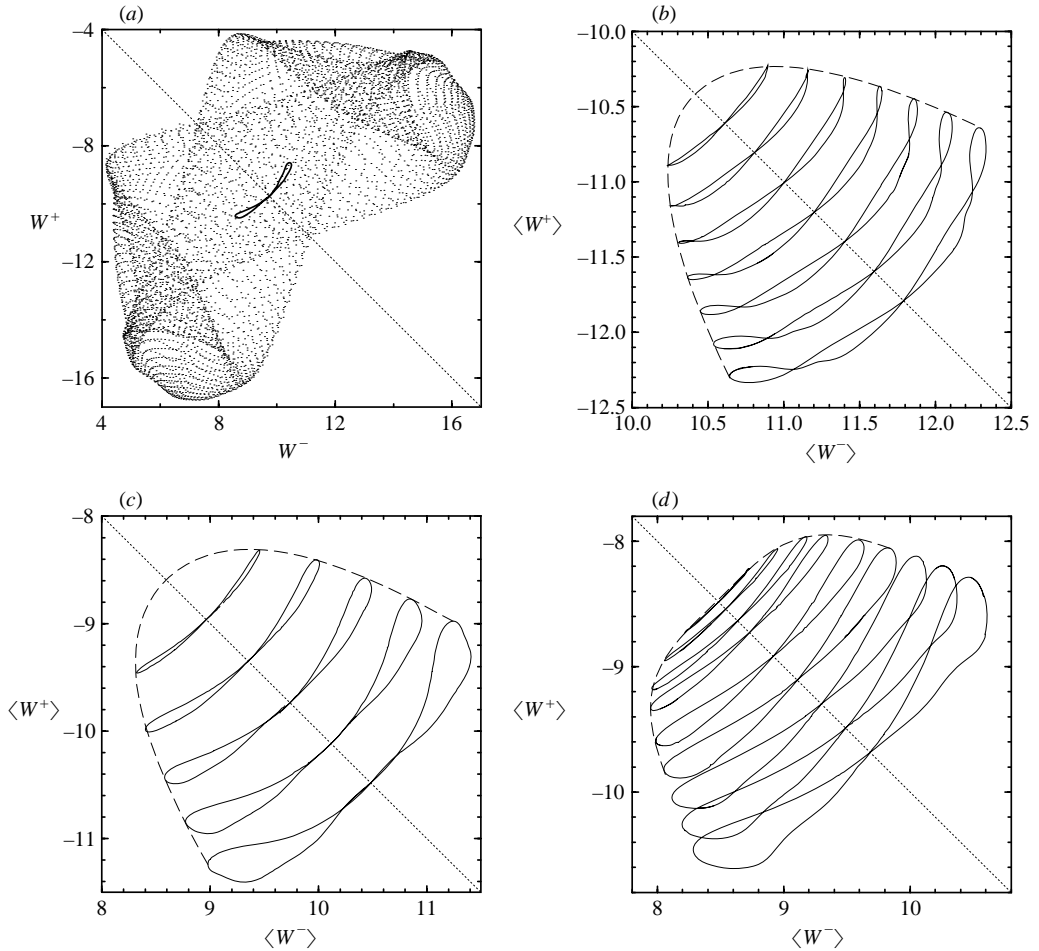
FIGURE 16. (*a*) Phase portrait (W^-, W^+) (dots) and filtered phase portrait $(\langle W^- \rangle, \langle W^+ \rangle)$ (solid) of MRW$_S$ for $\Gamma = 3.12$, $Re = 740$. (*b*) Filtered phase portraits of MRW$_S$ for $\Gamma = 3.0$ and $Re = 770$ to 830 in steps of 10. (*c*) Same as (*b*) for $\Gamma = 3.12$ and $Re = 700$ to 780 in steps of 20. (*d*) Same as (*b*) for $\Gamma = 3.16$ and $Re = 677$, 680, 685 and 690 to 740 in steps of 10. Dashed lines are quartic fits.

are the axial velocities at the points $(r = r_i/d + 1/2, \theta = 0, z = \pm\Gamma/2)$. The reflection symmetry of the phase portrait about the line $W^+ + W^- = 0$ is indicative of the Z_2 symmetry of the two-torus. The two-torus looks rather convoluted; this is because the fast frequency (corresponding to the precession frequency of the underlying RW$_S$ from which MRW$_S$ bifurcates) has large amplitude and the slow frequency (the modulation) has low amplitude since MRW$_S$ bifurcates supercritically. So, instead of the limit cycle 'shedding its skin' (which would give a two-torus that looks like a doughnut), in this case the limit cycle 'wobbles'. Now, the fast (precession) frequency $(2\pi/\tau)$ is a constant (in time) that depends only weakly on parameters, and so the phase dynamics associated with the underlying rotating wave component of MRW$_S$ are trivial and essentially decouple from the rest of the dynamics. This allows us to low-pass filter these solutions and extract a clearer picture of the dynamics. Given a function
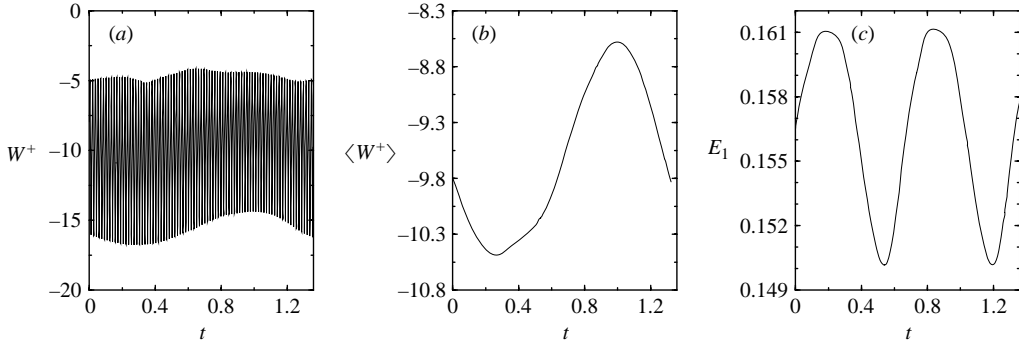
FIGURE 17. Time series of MRW$_S$ at $Re = 740$ and $\Gamma = 3.12$.

Γ	a	b	c
3.00	0.0998	0.950	14.73
3.12	0.1076	0.563	12.15
3.16	0.2735	−0.014	11.98

TABLE 1. Quadratic fits to the amplitudes of the filtered portraits of MRW$_S$ shown in figure 16: $y = ax^4 + bx^2 + c$, where $x = -(\langle W^+ \rangle + \langle W^- \rangle)/\sqrt{2}$, $y = -(\langle W^+ \rangle - \langle W^- \rangle)/\sqrt{2}$.

of time $f(t)$, the filtered function, $\langle f(t) \rangle$, is a running average defined as

$$\langle f(t) \rangle = \frac{1}{\tau} \int_{t-\tau/2}^{t+\tau/2} f(y)\,\mathrm{d}y, \tag{7.1}$$

where τ is the precession period associated with the rotating wave component of the solution considered. The modulation period, τ_2, is considerably longer, and is not filtered out.

Figure 17 illustrates the low-pass filtering of a MRW$_S$ solution at $Re = 740$ and $\Gamma = 3.12$. Part (a) of the figure is the time series of the axial velocity at a point W^+ over approximately one modulation period (about 1.4 viscous times). This modulation period is much greater than the underlying precession period (about 0.03 viscous time) which can only just be resolved in the plot. Applying the low-pass filter results in the periodic signal $\langle W^+ \rangle$ shown in part (b) of the figure. The corresponding time series of the modal energy E_1 is shown in part (c) of the figure; both $\langle W^+ \rangle$ and E_1 are periodic (the fast oscillations in W^+ are filtered out of $\langle W^+ \rangle$, and since the fast oscillations correspond to a precession they do not appear in E_1). The Z_2 symmetry of MRW$_S$ is responsible for the period of E_1 being half of that of $\langle W^+ \rangle$.

Figure 16(a) is a phase portrait of MRW$_S$ at $Re = 740$ and $\Gamma = 3.12$ projected onto (W^-, W^+) (dots) as well as its low-pass filter projected onto $(\langle W^- \rangle, \langle W^+ \rangle)$ (solid curve). The filtered portrait is a limit cycle of much smaller extent than the unfiltered portrait (the two-torus). The extent of the limit cycle is another measure of the modulation amplitude. In parts (b), (c) and (d) of figure 16 are filtered portraits of MRW$_S$ at $\Gamma = 3.00$, 3.12 and 3.16, respectively, for a number of Re values. The filtered phase portraits of RW$_S$ from which the MRW$_S$ bifurcate are points that lie on the line $\langle W^+ \rangle = -\langle W^- \rangle$. The dashed curves enveloping the MRW$_S$ filtered portraits are curve fits of the form $y = ax^4 + bx^2 + c$, where $x = -(\langle W^+ \rangle + \langle W^- \rangle)/\sqrt{2}$ and $y = -(\langle W^+ \rangle - \langle W^- \rangle)/\sqrt{2}$. The values of the fitted coefficients are listed in table 1. The
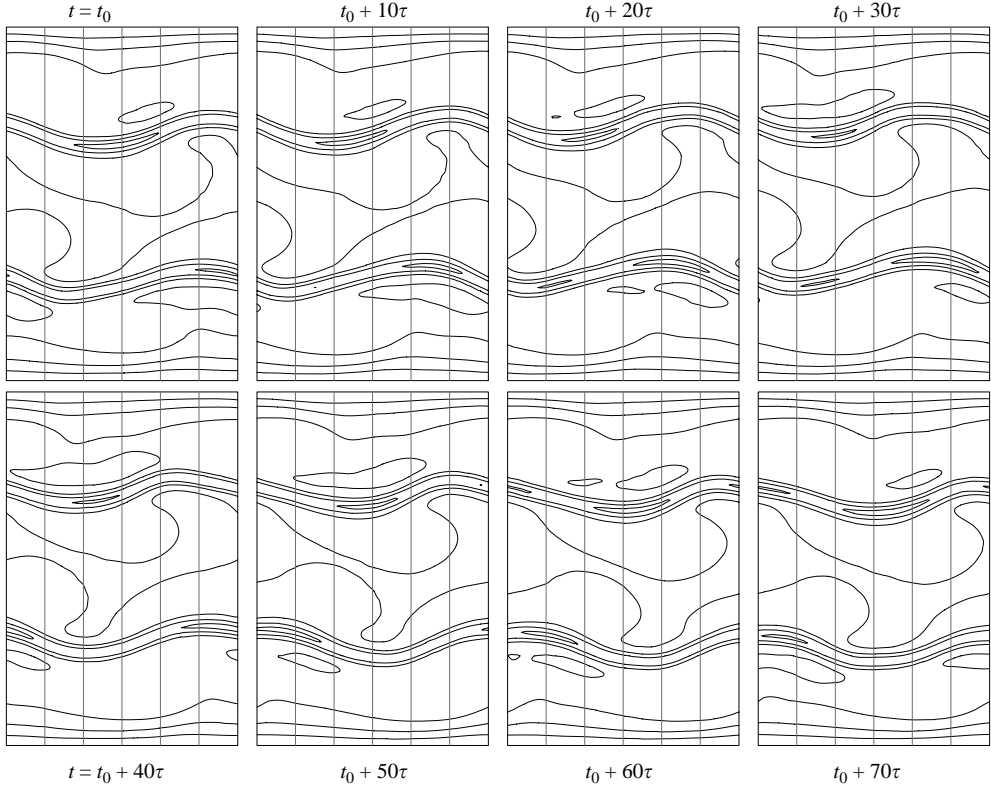
FIGURE 18. Contours of v in the cylindrical plane $r = r_i/d + 0.3$ of MRW$_S$ at $Re = 740$, $\Gamma = 3.12$, $\eta = 0.5$. The sequence covers (approximately) one modulation period τ_2, and the frames are ten precession periods apart (10τ). There are twelve equispaced contours with the levels $v \in [0, Re]$. Vertical lines at angles $\theta = j\pi/3$ for $j = 1$ to 5 are included.

fit for $\Gamma = 3.00$, and to a slightly lesser degree for $\Gamma = 3.12$, is quadratic, typical of a supercritical Neimark–Sacker bifurcation. For $\Gamma = 3.16$ however, the quartic term dominates and we find that the Neimark–Sacker bifurcation is slightly subcritical.

The Floquet multipliers for the Neimark–Sacker bifurcation are complex conjugates of the form $\mu = \exp(\pm i\alpha)$, and the modulation period is of the form $\tau_2 = (2\pi/\alpha)\tau$, where τ is the period of the limit cycle from which the quasi-periodic solution bifurcates. For MRW$_S$, we have shown (figure 15) that as Γ increases beyond about 3.15, $\tau_2 \to \infty$ so that $\alpha \to 0$ and $\mu \to +1$. So, not only is the Neimark–Sacker bifurcation becoming subcritical, it is also becoming degenerate as $\Gamma \to 3.18$.

Figure 18 shows the jet dynamics associated with the modulation period τ_2, for MRW$_S$ at $Re = 740$, $\Gamma = 3.12$, $\eta = 0.5$; this is the same MRW$_S$ as shown in figures 16(*a*) and 17. The figure shows contours of v in the cylindrical plane $r = r_i/d + 0.3$, strobed every ten precession periods; in fact we have computed Poincaré sections of MRW$_S$ and recorded the velocity field every time it crosses the section given by $U^+ = -20.0$ (where U^+ is the radial velocity at the point $r = r_i/d + 1/2$, $\theta = 0$, $z = \Gamma/2$). The modulation period is $\tau_2 = 1.31$, while the precession period is $\tau = 0.0164$; there are $\tau_2/\tau = 80.3$ precession periods in every modulation period. Figure 18 consists of eight frames that are 10 precession periods apart, and hence it very nearly covers one modulation period τ_2. In the three first frames the upper jet phase (position of the
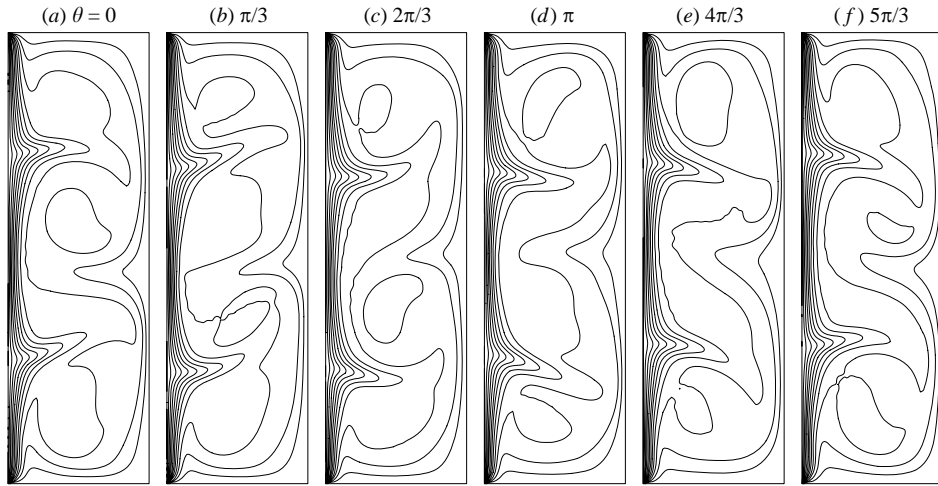
FIGURE 19. Contours of v in various meridional plane, as indicated, for RW$_A$ at $Re = 700$, $\Gamma = 3.20$, $\eta = 0.5$; computed with $N_z = 96$, $N_r = 48$, $N_\theta = 20$, $\delta t = 2 \times 10^{-5}$. There are twelve positive contours with the levels $v \in [0, Re]$.

maxima and minima) is advanced in θ with respect to the lower jet. In frames five to seven, the opposite is true. In frames 4 and 8 the two jets are almost in phase. Therefore, the dynamics associated with the Neimark–Sacker bifurcation correspond to an oscillation of the relative phase between the upper and lower jets, with period τ_2. The flow is no longer Z_2-symmetric, but the two-tori on which it evolves are Z_2-symmetric. This is clearly seen in figure 18: the frames in the second row are almost exactly the axial reflection ($z \to -z$) of the corresponding frames in the first row, with an appropriate rotation in the azimuthal direction. But the quasi-periodic character of the solution (it never repeats itself if the frequencies are incommensurate) prevents an individual MRW$_S$ solution from having an exact spatio-temporal Z_2 symmetry.

7.2. Cyclic pitchfork bifurcation of RW$_S$

We now turn our attention to the instability of RW$_S$ for $\Gamma > 3.18$, which is due to a pitchfork bifurcation breaking Z_2 symmetry. Figure 19 shows contours of the azimuthal velocity v of one of the pair of bifurcating rotating waves RW$_A$, which has azimuthal wavenumber $m = 1$, at $Re = 700$ and $\Gamma = 3.20$ in various meridional planes. Figure 20 shows the same contours on a cylindrical surface (θ, z) at $r = r_i/d + 0.3$, projected on a plane and compressed in azimuth by a factor of four in order to better display the structure of the tilt wave. The lack of reflection symmetry about $z = 0$ is immediately obvious (as it was for RW$_S$), but unlike RW$_S$, RW$_A$ is not invariant to a reflection composed with a rotation through π. In essence, the Z_2 symmetry breaking corresponds to the two jets emerging from the inner cylinder boundary layer being tilted out of phase with respect to each other (the tilts are in-phase for RW$_S$). From the figure, one can see that the phase difference is about $2\pi/9$ ($40°$) for this case. The corresponding Z_2-conjugate RW$_A$ is the reflection of RW$_A$ through $z = 0$, so that the phase difference between the tilts of the top and bottom jets is the negative of that of its partner.

To obtain a quantitative measure of the breaking of Z_2 symmetry (consisting of the combination of the z-reflection and an azimuthal rotation of π/m) of RW$_A$ (which
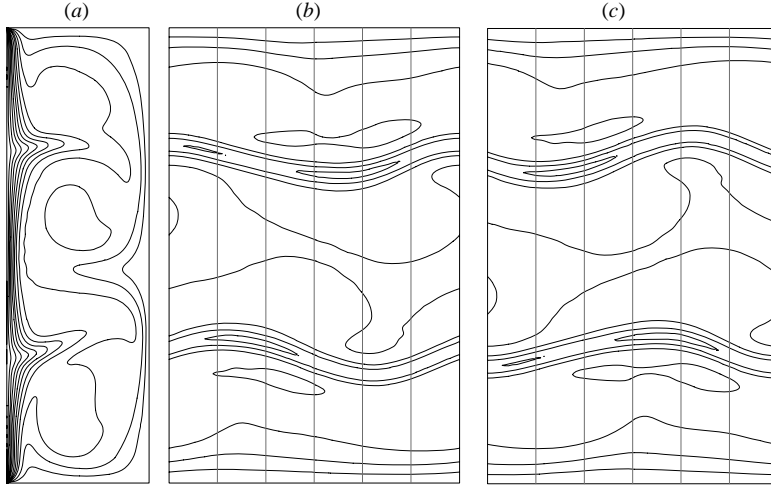
FIGURE 20. Contours of v in (*a*) the meridional plane $\theta = 0$, and (*b*) the cylindrical projection (θ, z) at $r = r_i/d + 0.3$, for RW$_A$ at $Re = 700$, $\Gamma = 3.2$, $\eta = 0.5$. Vertical lines at angles $\theta = j\pi/3$ for $j = 1$ to 5 are included in (*b*), which correspond to the meridional planes used in figure 19. There are twelve equispaced contours with the levels $v \in [0, Re]$. (*c*) The Z_2-conjugate state of (*b*).
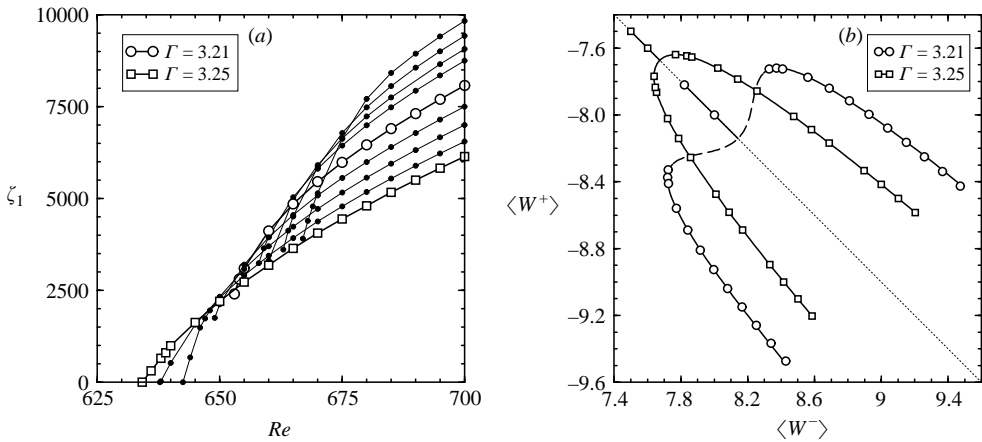

FIGURE 21. (*a*) Variation of ζ_1 for RW$_A$ with Re for $\Gamma = 3.188$, 3.192, 3.196 and 3.20 to 3.25 in steps of 0.01. (*b*) Filtered phase portraits of RW$_S$ and RW$_A$ at $\Gamma = 3.21$ and 3.25 and for Re values corresponding to the respective Γ curves in (*a*). Symbols correspond to computed solutions and lines are quartic fits.

has $m = 1$), we introduce a parameter ζ_m:

$$\zeta_m = \sum_{j=0}^{N_r} \sum_{k=-N_\theta}^{N_\theta} \left[\sum_{i=0}^{N_z/2} |w_{2i,j,k}|^2 \cos^2\left(\frac{k\pi}{2m}\right) + \sum_{i=0}^{(N_z-1)/2} |w_{2i+1,j,k}|^2 \sin^2\left(\frac{k\pi}{2m}\right) \right]. \quad (7.2)$$

This parameter is zero when the rotating wave is Z_2 symmetric. ζ_m is a global measure of the velocity squared, and so at a supercritical pitchfork bifurcation, ζ_m of RW$_A$ should grow linearly with distance in parameter space from the bifurcation curve.

Figure 21(*a*) shows the variation with Re of ζ_1 for RW$_A$ at various Γ, from $\Gamma = 3.188$ to 3.25. For $\Gamma = 3.23$, 3.24 and 3.25, we have been able to continue
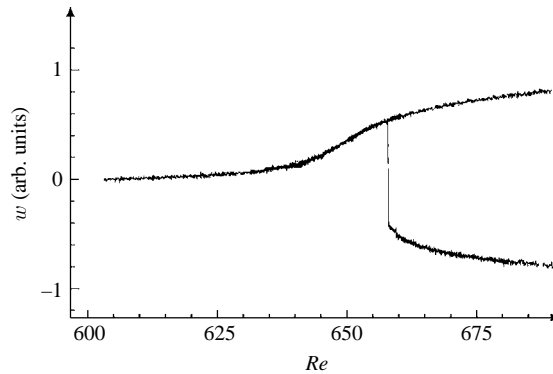
FIGURE 22. Measurement of axial velocity w in the axial midplane showing an imperfect pitchfork bifurcation in the experiments at $\Gamma = 3.208$. Lower border of decoupled branch provides a measure of the location of the fold bifurcation.

RW$_A$ solutions with decreasing Re all the way to the pitchfork bifurcation where $\zeta_1 \to 0$. However, for $\Gamma \leqslant 3.22$, below a certain value of Re (dependent on Γ) the flow started with an initial condition corresponding to RW$_A$ with finite ζ_1 at a slightly larger Re evolves to RW$_S$. This behaviour is indicative of a saddle-node (cyclic fold, CF) bifurcation of RW$_A$, and hence that the cyclic pitchfork bifurcation is subcritical for $\Gamma \leqslant 3.22$. In figure 21(b), we plot the filtered phase portraits of RW$_S$ and RW$_A$ at $\Gamma = 3.21$ and 3.25 for a range of Re (roughly between 620 and 700). The low-pass filtering results in these phase portraits of rotating waves simply being fixed points. For RW$_S$, the phase portraits are fixed points on the line $\langle W^+ \rangle = -\langle W^- \rangle$, and for RW$_A$ and its Z_2-conjugate the portraits are a pair of points symmetric about this line. For $\Gamma = 3.25$, the locus of phase portraits of RW$_A$ lies on a parabola about the line $\langle W^+ \rangle = -\langle W^- \rangle$, giving the usual picture of a supercritical pitchfork bifurcation. For $\Gamma = 3.21$, a quartic fit to the RW$_A$ points shows the typical form of a subcritical pitchfork bifurcation.

Due to unavoidable imperfections in the apparatus, the experiment does not have a perfect Z_2 symmetry and it is well known that imperfections may alter the structure of Z_2 symmetry-breaking bifurcations. Figure 22 depicts a bifurcation diagram of an imperfect cyclic pitchfork obtained experimentally at $\Gamma = 3.208$. It is measured by a quasi-static variation of Re while recording the axial velocity w in the axial mid-plane at a radial distance of 1.5 mm from the inner cylinder. On increasing Re from subcritical values, the nominally symmetric RW$_S$ is smoothly connected with an asymmetric RW$_A$. The conjugate decoupled asymmetric RW$_A$ (which is arrived at by sudden changes in Re) disappears catastrophically as Re is decreased from supercritical values. The corresponding Re is taken as a measure of the cyclic fold bifurcation of the imperfect cyclic pitchfork bifurcation. Here, the critical Reynolds number is estimated to be $Re_c = 658.8$ for $\Gamma = 3.208$.

The experimental loci of the cyclic pitchfork bifurcations, shown in figure 13 as open diamonds, correspond to estimates of the fold resulting from the imperfect pitchfork bifurcation. The SNIP (open squares) and saddle-loop homoclinic (open triangles) bifurcations, also shown in figure 13, are only found to occur on the smoothly connected asymmetric branch. These bifurcations in the experiment are therefore homoclinic instead of heteroclinic bifurcations in a perfectly symmetric flow (such as in the numerics). The two experimental bifurcation lines shown, instead of
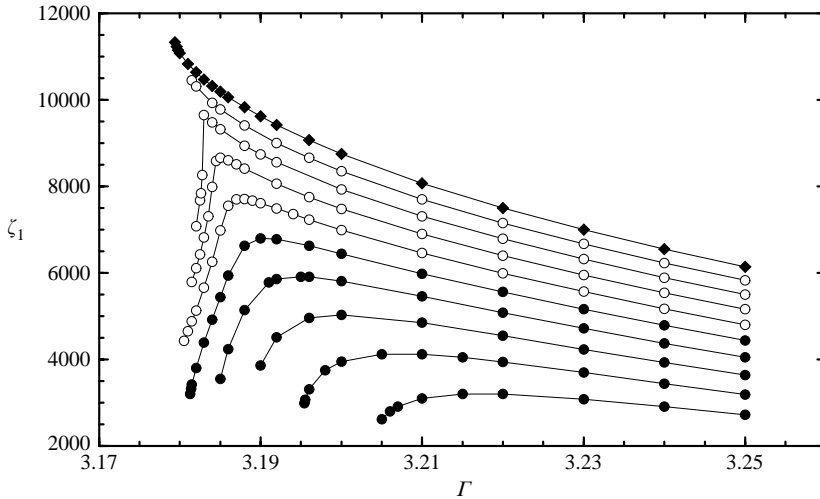
FIGURE 23. Variation of ζ_1 for RW_A with Γ for $Re \in [655, 700]$, in steps of 5. For $Re \in [655, 675]$ (filled circles), the RW_A undergo cyclic fold (CF) bifurcations at low Γ. For $Re \in [680, 695]$ (open circles), at low Γ RW_A undergoes Neimark–Sacker (NS$_a$) bifurcations spawning MRW_A. For $Re = 700$ (filled diamonds), the RW_A undergo a saddle-node-infinite-period (SNIP) bifurcation with another nearby saddle RW_A (actually there is a pair of stable/saddle RW_A due to the Z_2 symmetry). The heteroclinic connections between the RW_A lead to the MRW_S following the SNIP bifurcation.

one in the numerics, are a consequence of the imperfection in the experimental system. The global bifurcations are described in detail in § 8.

The ζ_1 variation with Γ of RW_A is shown in figure 23 for Re between 655 and 700. For $\Gamma > 3.22$, ζ_1 increases linearly with Re, but for smaller Γ, the behaviour of ζ_1 is quite varied. For Re between 655 and 675 (the curves with filled circles), RW_A terminates at a cyclic fold bifurcation as Γ is reduced (as discussed above). For Re between 680 and 695 (curves with open circles), as Γ is reduced, RW_A loses stability at a supercritical Neimark–Sacker bifurcation (NS$_a$) at which a modulated rotating wave MRW_A is spawned (there are a pair of Z_2-conjugate MRW_A bifurcating from the pair of RW_A). For $Re = 700$ and higher, instead of suffering the local NS$_a$ bifurcation, RW_A suffers a global bifurcation as Γ is reduced. In the following section we explore the nature of this global bifurcation as well as the fate of MRW_A.

8. Z_2 symmetry breaking via global bifurcations

Across a curve along $\Gamma \sim 3.18$ (see figure 13, which shows both the numerically and the experimentally determined curve), a complex symmetry-breaking bifurcation process takes place providing a connection between the Z_2-symmetric state (MRW_S) and the non-Z_2-symmetric states (either RW_A or MRW_A). For the connection between MRW_S and RW_A, this complex process involves a global SNIP (saddle-node-infinite-period) bifurcation with Z_2 symmetry.

The SNIP bifurcation consists of a saddle-node bifurcation taking place on a limit cycle, as shown schematically in figure 24(a). Before the bifurcation (left diagram), the period of the limit cycle tends to infinity as the bifurcation is approached, and the periodic solution spends more and more time near the place where the saddle-node will appear. The periodic solution becomes a homoclinic orbit at the bifurcation point
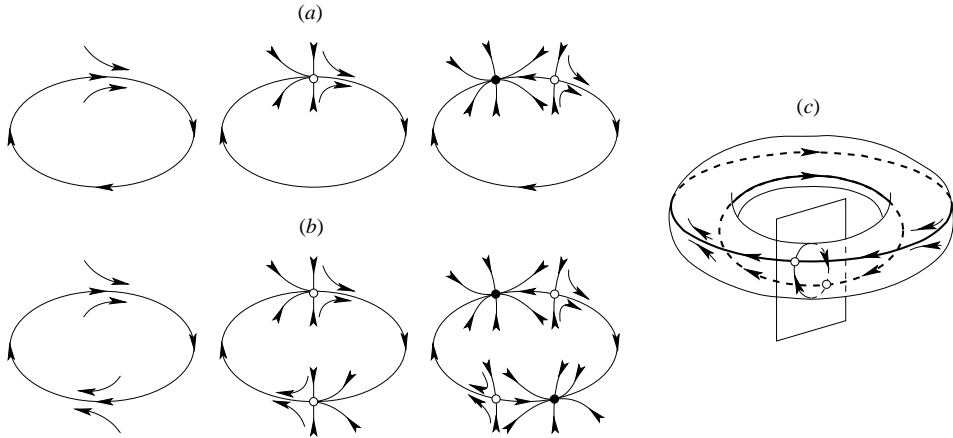
FIGURE 24. Schematic of the SNIP bifurcation on an invariant circle in (*a*) a generic system, and (*b*) a Z_2-symmetric system; left, central and right diagrams correspond to before, during and after the SNIP bifurcation. (*c*) Schematic of the SNIP bifurcation on an invariant two-torus; the planar section (a Poincaré section) corresponds to case (*b*) centre.
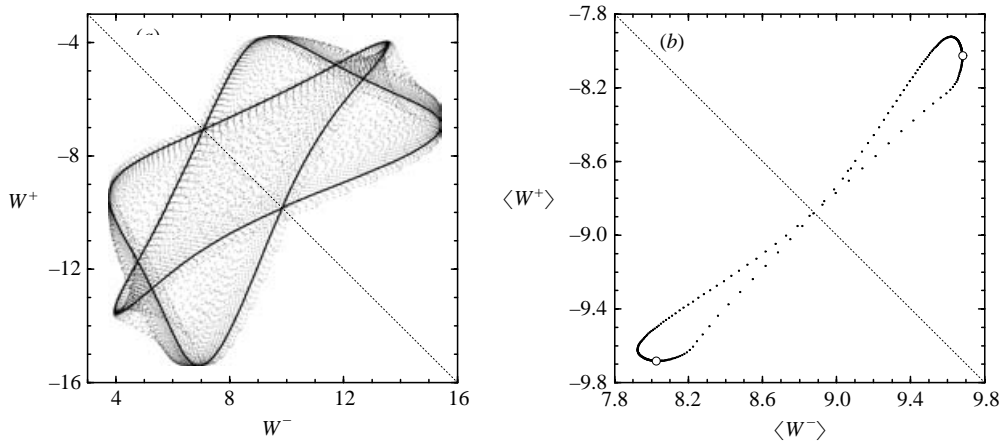

FIGURE 25. Phase portraits of the SNIP transition from MRW$_S$ to RW$_A$ at $Re = 700$, showing the MRW$_S$ for $\Gamma = 3.1785$ and the RW$_A$ for $\Gamma = 3.1793$. (*a*) Full solutions projected on the (W^-, W^+) plane. (*b*) Low-pass-filtered solutions projected on the $(\langle W^- \rangle, \langle W^+ \rangle)$.

(central diagram). After the bifurcation the periodic solution no longer exists and there remains a pair of fixed points, one a saddle (unstable, hollow in the figure) and the other a node (stable, solid in the figure). This is a codimension-one bifurcation (Kuznetsov 1998). In the presence of a Z_2 symmetry, if the limit cycle is not pointwise Z_2-invariant, then a pair of saddle-nodes appears simultaneously on the invariant circle, as shown schematically in figure 24(*b*). This is what happens in our problem, but instead of a limit cycle we have quasi-periodic solutions (a two-torus), as depicted schematically in figure 24(*c*). In this case the two saddle-nodes become saddle-nodes of limit cycles; the two Z_2-symmetric saddle-nodes at the bifurcation point are shown as thick lines. Figure 25(*a*) shows phase portraits of MRW$_S$ and RW$_A$ at $Re = 700$ to either side of the SNIP bifurcation ($\Gamma = 3.1785$ for MRW$_S$ and 3.1793 for RW$_A$). In part (*b*) of this figure are plotted the low-pass-filtered phase portraits of these
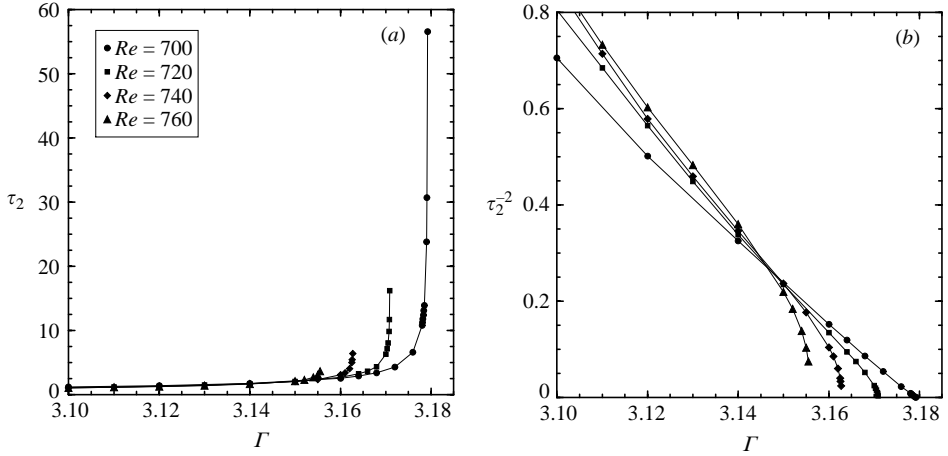
FIGURE 26. Variation with Γ of the modulation period, τ_2, of MRW$_S$ near the SNIP bifurcation, computed for Re as indicated.

solutions showing a situation essentially equivalent to that in the Poincaré section of figure 24(c).

As MRW$_S$ approaches the SNIP bifurcation, its modulation period τ_2 becomes infinite, following the typical inverse square-root law associated with saddle-nodes (Strogatz 1994). This behaviour is illustrated in figure 26. The scaling fits the data best for the lower Re because as Re is increased, there are other bifurcations taking place near the SNIP which affect the modulation period of MRW$_S$ (details of these will be presented elsewhere). The primary period, τ, remains close to the precession period of RW$_S$ from which MRW$_S$ bifurcates, varying by about 10 % over the parameter range considered here.

Focusing on the region where the SNIP, Neimark–Sacker and cyclic pitchfork bifurcation curves approach each other, we find that rather than meeting at a point, there is instead a small window in parameter space where transition between the symmetric and the non-symmetric states is accomplished via a pair of saddle-loop homoclinic (SLH) bifurcations. This window is too small to be seen well in figure 13, so a close-up view is presented in figure 27. As Γ is reduced, RW$_A$ suffer a Neimark–Sacker (NS$_a$) bifurcation spawning Z_2-conjugate MRW$_A$; the NS$_a$ bifurcation curve and the SLH bifurcation curve are separated by variations in aspect ratio Γ of about 0.03 %.

Figures 28(a) and 28(b) show low-pass-filtered phase portraits of the MRW$_S$, MRW$_A$, and RW$_A$ solutions found numerically in such a window. Part (a) shows the projection used earlier: $(\langle W^- \rangle, \langle W^+ \rangle)$. In this projection, the limit cycles are on a two-dimensional manifold that is essentially perpendicular to the projection plane, and so we do not see them very well (this part of the figure consists of MRW$_S$ at $\Gamma = 3.18062$ and the pair of Z_2-conjugate MRW$_A$ at $\Gamma = 3.18063$, all at $Re = 690$). The one good aspect of this projection is that the role of Z_2 symmetry in these solutions is immediately obvious. A better projection on which to see the phase portraits (although it loses the Z_2 symmetry information) is $(\langle U^+ \rangle, \langle V^+ \rangle)$, where U^+ and V^+ are the radial and azimuthal velocities at the point where the axial velocity W^+ is recorded. Part (b) of the figure is such a projection. The MRW$_S$ at $\Gamma = 3.18062$ is shown as dots, MRW$_A$ at Γ from 3.18063 to 3.1815 are shown as solid closed curves, and RW$_A$ at
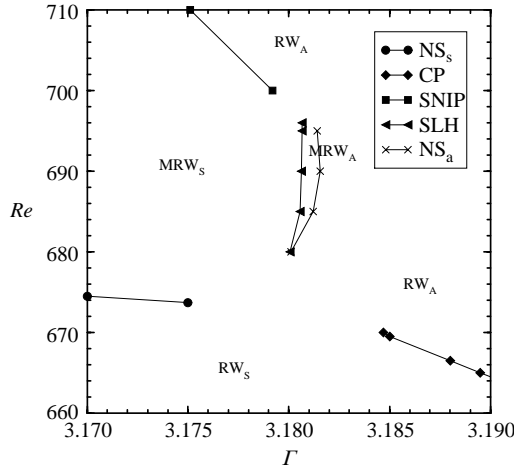
FIGURE 27. Close-up of the numerical bifurcation curves shown in figure 13, focusing in on the SLH bifurcation. Stable solutions in each region are indicated.
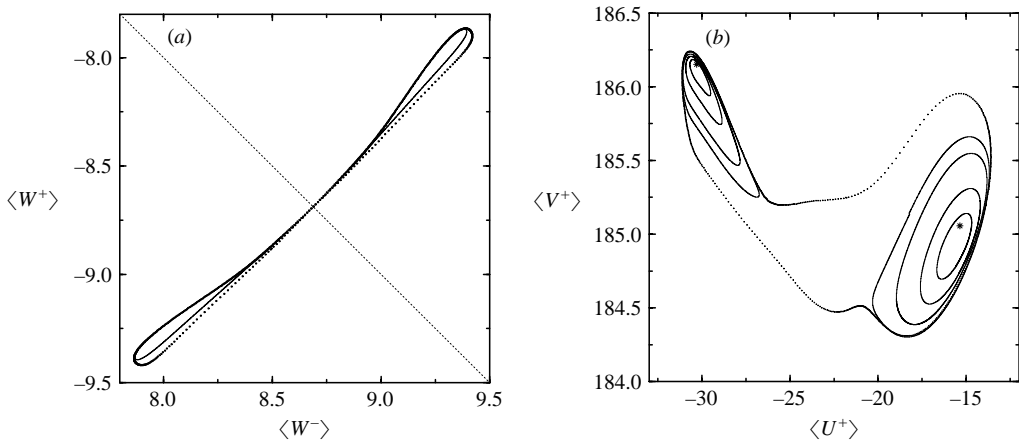

FIGURE 28. (*a*) Phase portraits projected on $(\langle W^-\rangle, \langle W^+\rangle)$ of MRW$_S$ at $\Gamma = 3.18062$ and MRW$_A$ at $\Gamma = 3.18063$, i.e. to either side of the SLH bifurcation. (*b*) Phase portraits projected on $(\langle U^+\rangle, \langle V^+\rangle)$ of MRW$_S$ at $\Gamma = 3.18062$, MRW$_A$ at $\Gamma = 3.18063, 3.1808, 3.1812$ and 3.1815, and RW$_A$ at 3.1820. All solutions have $Re = 690$.

$\Gamma = 3.1820$ are the pair of star symbols; all at $Re = 690$. In this projection, it is more clear that the pair of Z_2-conjugate MRW$_A$ undergoes SLH bifurcations with a pair of Z_2-conjugate saddle rotating waves (conjectured to appear at a secondary cyclic pitchfork bifurcation from RW$_S$) as Γ is reduced from 3.18063. Following the SLH bifurcation, the Z_2-symmetric MRW$_S$ results, which at $\Gamma = 3.18062$ is seen to be nearly heteroclinic to the same pair of Z_2-conjugate saddle rotating waves. The modulation periods of MRW$_S$ and MRW$_A$ grow unbounded. The computed values of these periods are shown in figure 29, with filled symbols for MRW$_S$ and open for MRW$_A$. One would expect these to following a log scaling law typical of SLH bifurcations (Strogatz 1994). However, the log fit depends critically on a good estimate of Γ_{crit} (where $\tau_2 \to \infty$), which is difficult and expensive to obtain numerically. Moreover, the close proximity of the Neimark–Sacker bifurcation NS$_a$ restricts the range of Γ where the scaling
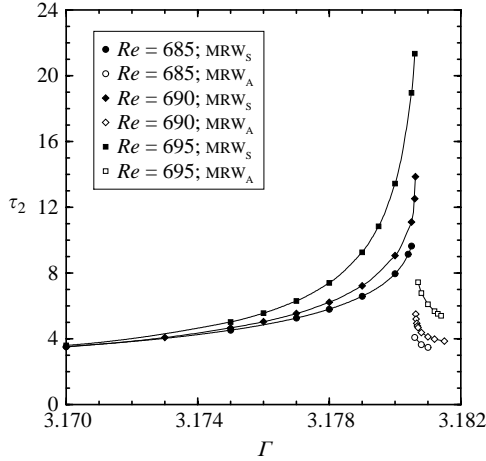
FIGURE 29. Variation with Γ of the modulation periods of MRW$_S$ (filled symbols) and MRW$_A$ (open symbols) near the SLH bifurcation, computed for Re as indicated.

would hold (one would need to get very close to the SLH bifurcation). For all these reasons, with the data obtained it is not possible to clearly distinguish between a log and an inverse square-root law close to Γ_{crit}.

Figure 30 shows the jet dynamics associated with the modulation period τ_2 for MRW$_A$ at $Re = 690$, $\Gamma = 3.18063$, and $\eta = 0.5$. This is the same MRW$_A$ as shown in figure 28. The figure shows contours of v in the cylindrical plane $r = r_i/d + 0.3$, strobed every 38 precession periods; the computed Poincaré section is the same as for MRW$_S$ ($U^+ = -20.0$). The modulation period is $\tau_2 = 5.51$, while the precession period is $\tau = 0.0175$; there are $\tau_2/\tau = 314.8$ precession periods in every modulation period; this ratio is so large because we are very close to the heteroclinic connection. Figure 30 consists of eight frames that are 38 precession periods apart, and hence it nearly covers one modulation period τ_2. The main differences with respect to MRW$_S$ (see figure 18) are that now the tilt of the upper jet is retarded in θ with respect to the tilt of the lower jet, while in MRW$_S$ it was advanced and retarded alternately in time. Moreover, the azimuthal positions of the jets (in the Poincaré section) are not fixed. They move in a certain interval of θ. This can be tracked by looking at the positions of the maximum values of v for each jet in the different frames (Poincaré sections). The length of the θ-interval for the lower jet is about $56°$, whereas for the upper jet it is about $40°$, clearly demonstrating the asymmetric nature of MRW$_A$ with respect to the reflection $z \to -z$. The MRW$_A$ exists for a very narrow range in Γ, and quickly reverts via a Neimark–Sacker bifurcation to a RW$_A$ with increasing Γ, in which the oscillation of the relative phase disappears; RW$_A$ has a fixed phase difference between the tilts of the top and bottom jets.

Details of the bifurcation structure shown in figure 27 are difficult to resolve with the present experimental apparatus. However, experimental evidence is found that the global Z_2 symmetry-breaking bifurcation from MRW$_S$ differs from a SNIP for lower Re. Figure 31 show experimental time series of low-pass-filtered LDV measurements of the axial velocity taken at $z = 0$ and $r = r_i + 1.5\,\mathrm{mm}$ for $Re = 684.4$ for various Γ between 3.162 and 3.171. The data presented have been low-pass filtered with a cut-off frequency of $0.5\,\mathrm{Hz}$ in order to filter out the precession frequency. The time series for $\Gamma = 3.162, 3.166$ and 3.168 show the very-low-frequency oscillations
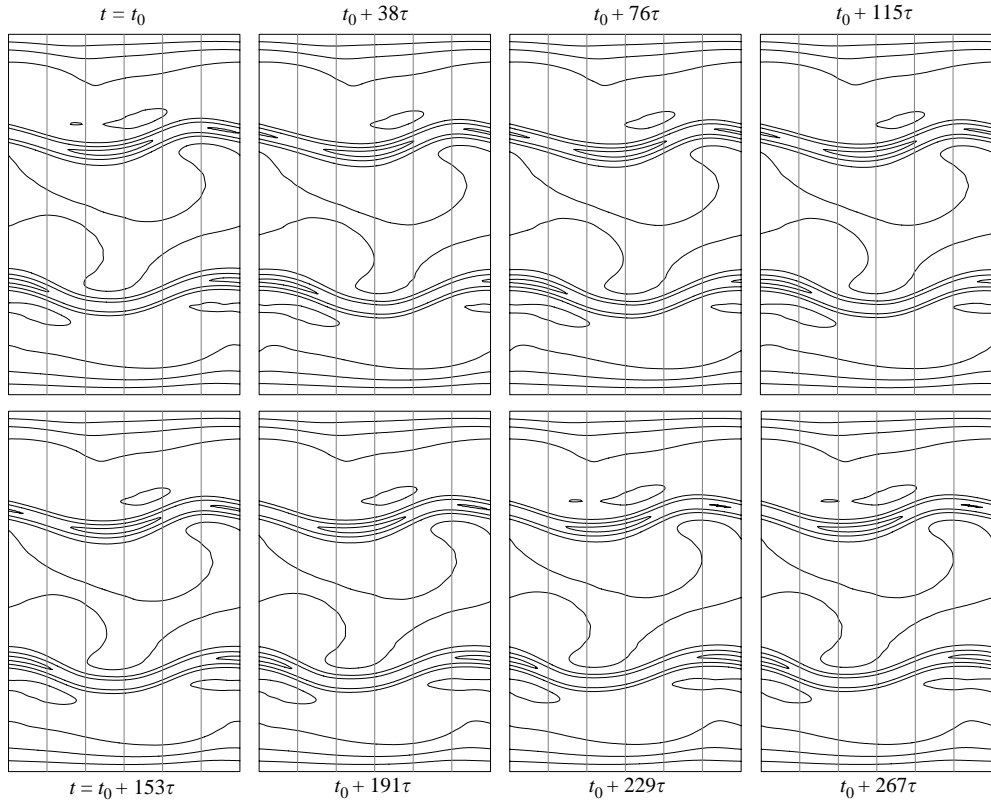
FIGURE 30. Contours of v in the cylindrical plane $r = r_i/d + 0.3$ of MRW$_A$ at $Re = 690$, $\Gamma = 3.18063$, $\eta = 0.5$. The sequence covers (approximately) one modulation period τ_2, and the frames are 38 precession periods apart (38τ). There are twelve equispaced contours with the levels $v \in [0, Re]$. Vertical lines at angles $\theta = j\pi/3$ for $j = 1$ to 5 are included.

Γ	Very-low frequency (Hz)	Precession frequency (Hz)
3.162	0.0171	4.0039
3.166	0.0134	4.0040
3.168	0.0085	4.0039
3.170	0.0093	4.0035
3.171	–	4.0054

TABLE 2. Frequencies of the flow states in figure 31.

of MRW$_S$ whose modulation frequency decreases rapidly with decreasing Γ as the global bifurcation is approached. The character of the time series at $\Gamma = 3.170$ is quite different, but there is still a very-low-frequency oscillation. This state is not space–time Z_2 symmetric; it is an MRW$_A$. At $\Gamma = 3.171$, the time series is essentially flat (aside from small-amplitude fluctuations due to experimental noise), and the flow state corresponds to RW$_A$. Table 2 provides the underlying precession periods of all these states as well as the very-low frequencies of the modulated waves. These results provide experimental evidence that the SLH scenario found numerically is physically robust, even though the details are not fully resolved experimentally.
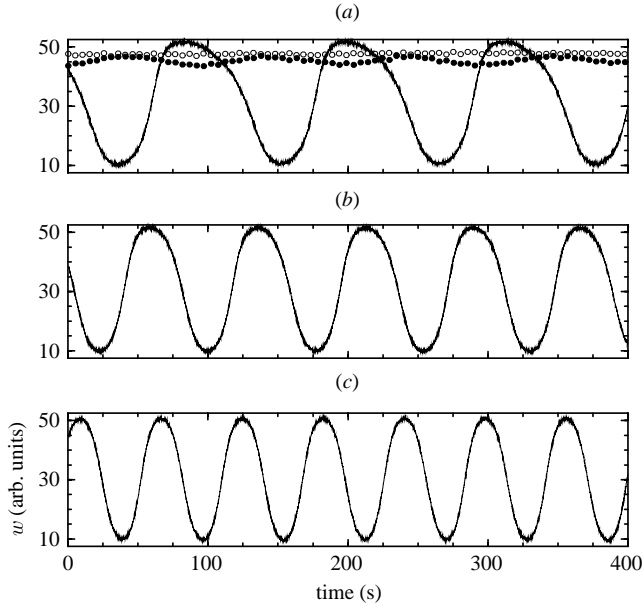
FIGURE 31. Experimentally measured time series (in seconds) of the axial velocity at $Re = 684.4$ and (a) $\Gamma = 3.171$ (RW$_A$, open circles), $\Gamma = 3.170$ (MRW$_A$ filled circles), $\Gamma = 3.168$ (MRW$_S$, black curve), (b) $\Gamma = 3.166$ (MRW$_S$), and (c) $\Gamma = 3.162$ (MRW$_S$).

9. Conclusions

Unfolding the bifurcation structure of a fluid flow generally provides deep insight into the organizing principles of complex dynamics. Our present study provides a bifurcation study of generic flow states in one of the classical hydrodynamic systems: rotating waves in Taylor–Couette flow. It reveals that rotating waves arising from instabilities of axisymmetric Taylor vortex flow can interact with Taylor vortex flow via a fold-Hopf bifurcation. The fold-Hopf bifurcation is responsible for the appearance of modulated rotating waves whose modulation oscillation develops into a very-low-frequency oscillation as the modulated waves suffer global bifurcations. In the parameter regimes we have studied here, the breaking of the midplane reflection symmetry plays a crucial role in the organization of the global bifurcations and the associated complicated dynamics.

Figure 32 summarizes the experimental and numerical results reported here. Taylor vortex flow solutions with one and two jets, s_1 and s_2, exist and are stable inside the broad wedged-shaped region delimited by a pair of saddle-node bifurcation curves which meet at the codimension-two cusp point. s_1 is stable in the parameter range studied, but s_2 loses stability via a symmetry-breaking Hopf bifurcation as Re is increased. The resulting rotating wave RW$_S$ interacts with the Taylor vortex steady solution s_2 at the fold-Hopf bifurcation, and loses stability at a subcritical Neimark–Sacker bifurcation for low Γ values. A narrow region of chaotic dynamics exists emerging from the fold-Hopf point, but in the present problem these dynamics are unstable (transient). On increasing Re beyond about 650, the rotating wave RW$_S$ undergoes two different bifurcations, depending on Γ. For $\Gamma < 3.18$ a Neimark–Sacker bifurcation takes place, resulting in a Z_2-symmetric two-torus T_s^2 with quasi-periodic solutions MRW$_S$. For $\Gamma > 3.18$, Z_2 symmetry is broken and a pair of asymmetric limit cycles, RW$_A$, appear in a cyclic pitchfork bifurcation.
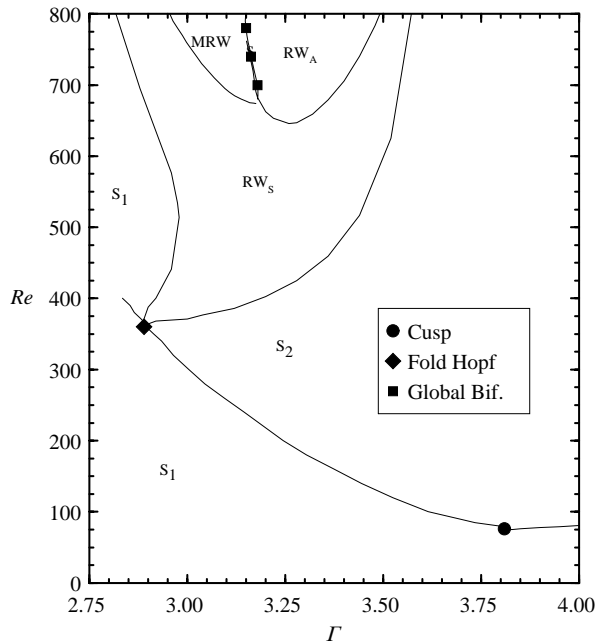
FIGURE 32. Numerically determined bifurcation curves shown over a broader parameter range.

Across a curve along $\Gamma \sim 3.18$ a complex symmetry-breaking bifurcation process takes place, providing a connection between the Z_2-symmetric state (MRW$_S$) and the non-Z_2-symmetric states (either RW$_A$ or MRW$_A$). For the connection between MRW$_S$ and RW$_A$, this complex process involves a global SNIP (saddle-node-infinite-period) bifurcation with Z_2 symmetry. Focusing on the region where the SNIP, Neimark–Sacker and cyclic pitchfork bifurcation curves approach each other, we find that rather than meeting at a point, there is instead a small window in parameter space where transition between the symmetric and the non-symmetric states is accomplished via a pair of saddle-loop homoclinic (SLH) bifurcations. Computations of the SLH scenario have been presented, and it has also been detected experimentally, providing experimental evidence that the SLH scenario is physically robust, even though the details are not fully resolved experimentally.

It is tempting to speculate that the global bifurcations appearing in the interaction between RW$_A$ and MRW$_S$ are in some way associated with the narrow wedge of chaotic dynamics emerging from the fold-Hopf bifurcation; even though these dynamics are unstable at low Re, they could manifest themselves when RW$_S$ becomes unstable at higher Re. This conjecture, however, is very difficult to explore. The numerical and experimental tools at our disposal are insufficient for the task.

In general, our results lend further support to the concept of how complex hydrodynamic behaviour results from mode interactions that lead to global bifurcations generating very-low-frequency dynamics. Of course, when present, symmetries are a natural source of multiple modes for the mode interaction, but similar complex behaviour in Taylor–Couette flow in the absence of midplane reflection symmetry has also been observed both experimentally and numerically to be organized by a fold-Hopf bifurcation (e.g. Mullin & Blohm 2001; Lopez *et al.* 2004*b*, where the top endwall was stationary and the bottom endwall rotated with the

inner cylinder). While organization via fold-Hopf bifurcations is quite common over an extensive part of parameter space in Taylor–Couette flows, it is not the exclusive organizing principle. In very-small-aspect-ratio Taylor–Couette flow, for example, Lopez & Marques (2003) have shown a very-low-frequency mode to be organized via the competition between two rotating waves resulting from a double-Hopf bifurcation.

What is becoming more apparent from the number of studies of bifurcations in Taylor–Couette flows where more than one governing parameter is varied is that there is not a single or even typical route to complex dynamics. Rather, the transition process is as rich and varied as the multiplicity of states that exist (Coles 1965). Nevertheless, the generic codimension-one local bifurcations (the saddle-node and the Hopf) and their codimension-two interactions – the cusp (collision between two saddle-node curves), the fold-Hopf (collision between a saddle-node curve and a Hopf curve), and the double-Hopf (collision between two Hopf curves) – provide the templates organizing much of the observed complex dynamics.

REFERENCES

ABSHAGEN, J., LOPEZ, J. M., MARQUES, F. & PFISTER, G. 2005 Symmetry breaking via global bifurcations of modulated rotating waves in hydrodynamics. *Phys. Rev. Lett.* **94**, 074101.

ABSHAGEN, J., PFISTER, G. & MULLIN, T. 2001 Gluing bifurcations in a dynamically complicated extended flow. *Phys. Rev. Lett.* **87**, 224501.

BENJAMIN, T. B. 1978a Bifurcation phenomena in steady flows of a viscous fluid. *Proc. R. Soc. Lond.* A **359**, 1–26.

BENJAMIN, T. B. 1978b Bifurcation phenomena in steady flows of a viscous fluid. II. Experiments. *Proc. R. Soc. Lond.* A **359**, 27–43.

BENJAMIN, T. B. & MULLIN, T. 1982 Notes on the multiplicity of flows in the Taylor experiment. *J. Fluid Mech.* **121**, 219–230.

BLACKBURN, H. M. & LOPEZ, J. M. 2002 Modulated rotating waves in an enclosed swirling flow. *J. Fluid Mech.* **465**, 33–58.

CHOSSAT, P. & IOOSS, G. 1994 *The Couette–Taylor Problem*. Springer.

COLES, D. 1965 Transition in circular Couette flow. *J. Fluid Mech.* **21**, 385–425.

CRAWFORD, J. D. & KNOBLOCH, E. 1991 Symmetry and symmetry-breaking bifurcations in fluid dynamics. *Annu. Rev. Fluid Mech.* **23**, 341–387.

DIPRIMA, R. C. & SWINNEY, H. L. 1981 Instabilities and transition in flow between concentric rotating cylinders. In *Hydrodynamics Instabilities and the Transtion to Turbulence* (ed. H. L. Swinney & J. P. Gollub). Topics in Applied Physics, vol. 45. Springer.

EGBERS, C. & PFISTER, G. (Eds.) 2000 *Physics of Rotating Fluids*. Lecture Notes in Physics, vol. 549. Springer.

GERDTS, U., VON STAMM, J., BUZUG, T. & PFISTER, G. 1994 Axisymmetric time-dependent flow in the Taylor-Couette system. *Phys. Rev.* E **49**, 4019–4026.

GUCKENHEIMER, J. & HOLMES, P. 1983 *Nonlinear Oscillations, Dynamical Systems, and Bifurcations of Vector Fields*. Springer.

IOOSS, G. & ADELMEYER, M. 1998 *Topics in Bifurcation Theory and Applications*, 2nd edn. World Scientific.

KEVREKIDIS, I. G., RICO-MARTÍNEZ, R., ECKE, R. E., FARBER, R. M. & LAPEDES, A. S. 1994 Global bifurcations in Raleigh–Bénard convection. Experiments, empirical maps and numerical bifurcation analysis. *Physica* D **71**, 342–362.

KNOBLOCH, E. 1994 Bifurcations in rotating systems. In *Lectures on Solar and Planetary Dynamos* (ed. M. R. E. Proctor & A. D. Gilbert), pp. 331–372. Cambridge University Press.

KRUPA, M. 1990 Bifurcations of relative equilibria. *SIAM J. Math. Anal.* **21**, 1453–1486.

KUZNETSOV, Y. A. 1998 *Elements of Applied Bifurcation Theory*, 2nd edn. Springer.

LOPEZ, J. M., HART, J. E., MARQUES, F., KITTELMAN, S. & SHEN, J. 2002*a* Instability and mode interactions in a differentially-driven rotating cylinder. *J. Fluid Mech.* **462**, 383–409.

LOPEZ, J. M. & MARQUES, F. 2003 Small aspect ratio Taylor-Couette flow: Onset of a very-low-frequency three-torus state. *Phys. Rev.* E **68**, 036302.

LOPEZ, J. M. & MARQUES, F. 2004 Mode competition between rotating waves in a swirling flow with reflection symmetry. *J. Fluid Mech.* **507**, 265–288.

LOPEZ, J. M., MARQUES, F. & FERNANDO, H. J. S. (Eds.) 2004*a Theoret. Comput. Fluid Dyn.; special issue Taylor-Couette Flows*, vol. 18(2–4). Springer.

LOPEZ, J. M., MARQUES, F. & SHEN, J. 2002*b* An efficient spectral-projection method for the Navier–Stokes equations in cylindrical geometries II. Three dimensional cases. *J. Comput. Phys.* **176**, 384–401.

LOPEZ, J. M., MARQUES, F. & SHEN, J. 2004*b* Complex dynamics in a short Taylor-Couette annulus with the top endwall stationary and the bottom rotating. *J. Fluid Mech.* **501**, 327–354.

LOPEZ, J. M. & SHEN, J. 1998 An efficient spectral-projection method for the Navier–Stokes equations in cylindrical geometries I. Axisymmetric cases. *J. Comput. Phys.* **139**, 308–326.

MARQUES, F., LOPEZ, J. M. & SHEN, J. 2002 Mode interactions in an enclosed swirling flow: a double Hopf bifurcation between azimuthal wavenumbers 0 and 2. *J. Fluid Mech.* **455**, 263–281.

MULLIN, T. 1982 Mutations of steady cellular flows in the Taylor experiments. *J. Fluid Mech.* **121**, 207–218.

MULLIN, T. 1991 Finite-dimensional dynamics in Taylor-Couette flow. *IMA J. Appl. Maths* **46**, 109–119.

MULLIN, T. 1993 *The Nature of Chaos*. Oxford University Press.

MULLIN, T. & BLOHM, C. 2001 Bifurcation phenomena in a Taylor-Couette flow with asymmetric boundary conditions. *Phys. Fluids* **13**, 136–140.

MULLIN, T., TAVENER, S. J. & CLIFFE, K. A. 1989 An experimental and numerical study of a codimension-2 bifurcation in a rotating annulus. *Europhys. Lett.* **8**, 251–256.

MULLIN, T., TOYA, Y. & TAVENER, S. J. 2002 Symmetry breaking and multiplicity of states in small aspect ratio Taylor-Couette flow. *Phys. Fluids* **14**, 2778–2787.

NORE, C., TUCKERMAN, L. S., DAUBE, O. & XIN, S. 2003 The 1:2 mode interaction in exactly counter-rotating von Karman swirling. *J. Fluid Mech.* **477**, 51–88.

PEACOCK, T. & MULLIN, T. 2001 Homoclinic bifurcations in a liquid crystal flow. *J. Fluid Mech.* **432**, 369–386.

PRICE, T. J. & MULLIN, T. 1991 An experimental observation of a new type of intermittency. *Physica* D **48**, 29–52.

VON STAMM, J., GERDTS, U., BUZUG, T. & PFISTER, G. 1996 Symmetry breaking and period doubling on a torus in the VLF regime in Taylor–Couette flow. *Phys. Rev.* E **54**, 4938–4957.

STROGATZ, S. 1994 *Nonlinear Dynamics and Chaos*. Addison-Wesley.

SWIFT, J. W. & WIESENFELD, K. 1984 Suppression of period doubling in symmetric systems. *Phys. Rev. Lett.* **52**, 705–708.

TAGG, R. P. 1994 The Couette-Taylor problem. *Nonlinear Sci. Today* **4**, 1–25.

TUCKERMAN, L. S. & BARKLEY, D. 1988 Global bifurcation to traveling waves in axisymmetric convection. *Phys. Rev. Lett.* **61**, 408–411.

WIGGINS, S. 1988 *Global Bifurcations and Chaos*. Springer.